ARCHIVES OF MECHANICS
Arch. Mech. **78** (∗), ∗∗∗–∗∗∗, 2026, https://doi.org/10.24423/aom.4893

Quasi-static compression and energy absorption performance of a hexa-arm honeycomb with different arrangement pattern

W. WANG[1,2∗)], Y. ZHANG[1)], X. SONG[1)]

[1)] *Department of Engineering Mechanics, School of Civil Engineering and Architecture, Henan University of Science and Technology, Luoyang 471023, China; e-mail: wswang@live.cn (corresponding author)*
[2)] *State Key Laboratory of Structural Analysis, Optimization and CAE Software for Industrial Equipment, Dalian University of Technology, Dalian 116023, China*

A hexa-arm honeycomb unit cell derived from a traditional honeycomb structure is proposed in this study. Through the periodic arrangement of the unit cell in a two-dimensional plane, four distinct honeycomb configurations are constructed: high density hexa-arm honeycomb (HHAH), orthogonal hexa-arm honeycomb (OHAH), inclined hexa-arm honeycomb (IHAH), and staggered distributed hexa-arm honeycomb (SHAH). Their deformation patterns and compression behaviors under quasi-static in-plane compressive loading are systematically investigated. Specimens are fabricated using 3D printing and subjected to quasi-static compression tests, numerical simulation models are established to validate the experimental results. Quantitative validation shows good agreement between experiments and simulations with high repeatability. The SHAH structure exhibits superior mechanical properties: compared with a conventional hexagonal honeycomb, its specific energy absorption is up to 155% higher. All four structures show positive Poisson's ratios. The hexa-arm honeycomb demonstrates a dual-stage deformation pattern during compression: the initial elastic stage is characterized by coordinated deformation of the entire structure, whereas further compression transitions into a second stage involving local failure or layer-by-layer collapse. The effects of different structural parameters on deformation patterns and specific energy absorption are also explored. These research findings provide valuable references for engineering applications of this type of honeycomb structure.

Key words: hexa-arm honeycomb, arrangement pattern, quasi-static compression, specific energy absorption.

1. Introduction

Honeycomb materials are porous biomimetic materials characterized by a two-dimensional lattice exhibiting a periodic topological arrangement within the plane, with parallel stacking layers extending out of the plane. Compared to conventional solid materials, honeycomb structures exhibit high porosity and low mass density, thereby demonstrating lightweight properties, high stiffness, and excellent energy absorption capability. These mechanical advantages have led to their widespread application in aerospace, marine engineering, automotive manufacturing, biomedical engineering, and sports equipment sectors [1–5]. For instance, in aerospace applications, honeycomb structures are employed in components such as fuselages, wings, and bulkheads [6], significantly reducing their weight while enhancing fuel efficiency and structural stability. In naval engineering, the outstanding impact resistance of honeycomb materials makes them common in critical structures, such as deck beams and hull walls [7–9]. In the automotive industry, honeycomb structures are employed in lightweight body and passenger compartment designs [10], effectively enhancing the structural safety and energy economy [11]. Notably, distinct application domains impose different demands on the mechanical properties of honeycomb structures: the aerospace sector prioritizes compressive and flexural strengths, whereas marine engineering places greater emphasis on impact resistance. To fulfil these specific requirements, a precise mechanical analysis of honeycomb structures is essential, along with optimized design approaches tailored to different operational contexts.

The application of honeycomb structures dates back nearly seven decades, during which scholars have conducted systematic investigations into their sandwich structures and mechanical properties, from the macro to micro scales. Numerous reviews have summarized relevant findings from diverse perspectives. Some studies have systematically reviewed advances in optimizing the mechanical properties of honeycomb structures [12, 13], whereas others have drawn inspiration from the geometric configurations of natural honeycomb structures, revealing their potential for structural optimization and material innovation [14]. Research on chiral honeycomb structures has focused on their characteristics, such as vibration, acoustic wave attenuation, impact energy absorption, and negative thermal expansion coefficients [15, 16]. The properties, fabrication techniques, and engineering applications of stretchable metamaterials and their derivative structures have also been comprehensively reviewed [17]. Despite decades of accumulated research, determining the key mechanical properties of honeycomb structures remains a significant challenge due to the diversity of their lattice shapes, configurations, and material types. The accurate prediction of these properties is crucial for their application in complex engineering scenarios.

Traditional honeycomb structures typically comprise periodically arranged hexagonal cells, with adjacent cells interconnected to form a continuous space [18–20]. Moreover, distinct unit cell geometries, such as stellate, square, and cruciform configurations, significantly influence the mechanical properties and energy absorption capacity [21–24]. By modifying the cell structures, the mechanical performance can be customized [25–29], rendering them particularly suitable for applications such as composite sandwich core materials, where exceptionally high energy absorption-to-weight ratios are achieved [30, 31]. Chen *et al.* [32]

analyzed the influence of the in-plane shear modulus and the unit cell geometry on the honeycomb behavior under in-plane compression based on the cellular material theory. QI *et al.* [33] compared the performance of honeycomb sandwich panels with re-entrant hexagonal unit cells via blast impact tests, and demonstrated a superior energy absorption capacity for the stiffener-enhanced structure compared to the conventional honeycomb. DONG *et al.* [34] systematically investigated the influence of cell wall thickness on honeycomb deformation patterns. Through quasi-static compression tests, they validated the significant differences in the deformation behavior between thin-walled and thick-walled honeycomb structures. By comparing the finite element analysis with the experimental results, the effect of the cell number on the honeycomb compression deformation and collapse behavior was explored. SIMSEK and EVIS [35] conducted multiparameter experiments and finite element simulations on the lattice structure of super-expanded honeycomb cores and investigated the regulatory mechanisms of the mechanical properties through variations in single-cell parameters. ARQUILLA *et al.* [36] conducted a comparative analysis of the compressive behavior of aluminum honeycombs under pure stress, combined stress, and shear stress, and investigated the distinct deformation modes of cells during combined compression. The study revealed that as the load application angle increased, both the shear resistance of the honeycomb and the tangential displacement at densification reached higher values.

The choice of material for preparing honeycomb cells is a key factor influencing their mechanical and energy absorption properties. Inspired by the microstructure of wood, UFODIKE *et al.* [24] compared the mechanical responses of honeycomb structures fabricated from different materials under in-plane compression and confirmed that the material selection significantly affects the honeycomb performance. YU *et al.* [37] analyzed the linear elastic response and collapse behavior of honeycombs under out-of-plane compression conditions using both theoretical and experimental approaches. MOAT *et al.* [38] inspired by the non-periodic Penrose P3 structure, designed a P3-based non-periodic honeycomb that demonstrated superior isotropic performance compared to traditional periodic square and hexagonal honeycombs. SHEN and LI [39] utilized an interpenetrating epoxy resin to construct a non-uniform three-dimensional ceramic lattice structure, significantly enhancing the energy absorption and load-bearing capacity. GAO *et al.* [40] demonstrated the superior mechanical properties and enhanced energy absorption capacity of novel structures through quasi-static compression testing and numerical simulation of board-based lattices with varying densities. WANG *et al.* [41] designed and fabricated shell-spike matrix structures with highly tunable anisotropy, investigated the influence of anisotropy on compressive mechanical behavior, and showed that the material orientation could be adjusted to adapt to loading conditions. GIBSON and ASHBY [42] systematically investigated the effects of the material type and structural parameters on the mechanical properties and energy absorption characteristics of honeycombs across different orientations. Yadav *et al.* [43] investigated a Ti64-Zn MBMV bimetallic composite and successfully incorporated Zn into the Ti64 honeycomb nail structure, demonstrating that this novel honeycomb scaffold holds promise as a next-generation biodegradable implant.

However, traditional honeycomb manufacturing processes, such as forming, bonding, welding, and extrusion, are only suitable for preparing simple honeycomb configurations and struggle to accommodate novel honeycomb structures with complex geometries [44–46]. Fortunately, the rapid advancement of 3D printing technology has opened new avenues for the design and fabrication of complex geometric unit cell structures [47, 48]. Wadley *et al.* [49] employed a combination of topology optimization and additive manufacturing to produce metal sandwich panels featuring periodic open-core configurations, thereby pioneering a low-cost approach for manufacturing high-strength lightweight structures. Mondal *et al.* [50] employed direct-injection welding 3D printing to fabricate diverse medium-to high-strength short carbon-fiber-reinforced epoxy composite honeycomb structures. This approach achieved the desired shear-thinning behavior and high-precision formation of complex geometries, demonstrating the significant influence of geometry on the structural strength. Guo and Sun [51] designed and fabricated four non-periodic honeycomb metamaterials via 3D printing, which significantly enhanced the stiffness of the honeycomb cells. Xia *et al.* [52] employed 3D printing to produce a novel double-layered helical honeycomb structure. The mechanical properties and energy absorption capacity were effectively enhanced by incorporating a helical hierarchical design into the honeycomb cells. Khaghanifard *et al.* [53] fabricated the TFGMEEEH collector using the reentrant negative Poisson ratio honeycomb and demonstrated that the negative Poisson ratio honeycomb exhibited higher power generation under identical conditions.

Based on conventional honeycomb structures, researchers have designed various modified honeycomb configurations to enhance their structural and mechanical properties [54–57]. However, most existing studies have focused on altering the unit cell geometry while maintaining a periodic arrangement. This study adopts a different perspective. Firstly, a previously unexplored hexa-arm honeycomb unit cell is proposed, by performing rotational transformations and spatial combinations on traditional honeycomb structures. Secondly, rather than adopting a single periodic layout, four distinct arrangement patterns derived from the same hexa-arm unit cell were constructed and compared: high-density hexa-arm honeycomb (HHAH), orthogonal hexa-arm honeycomb (OHAH), inclined hexa-arm honeycomb (IHAH), and staggered distributed hexa-arm honeycomb (SHAH). Thirdly, the combined experimental and numerical simulation approach was employed to systematically study the deformation mechanisms, in-plane compression behavior, and energy absorption capacity of these structures under quasi-static in-plane compression. The corresponding specimens were fabricated using 3D printing, and the influence of key structural parameters on mechanical performance was examined. The results provide a valuable reference for engineering applications of hexa-arm honeycomb structures.

2. Hexa-arm honeycomb structure design and analysis methods

2.1. Structure design

A novel hexa-arm honeycomb unit cell was constructed by taking a regular hexagon and its six adjacent edges from the conventional two-dimensional honeycomb structure. Through geometric transformations, namely rotation and translation, each adjacent edge is vertically and equally bisected into the corresponding side of the hexagon, as shown in Fig. 1. The geometric dimensions of the unit cell are defined by two key parameters: the radius R of the inscribed circle of the wall and arm thickness t. In the preliminary study, the specific parameter values were set to $R = 4$ mm and $t = 1$ mm.

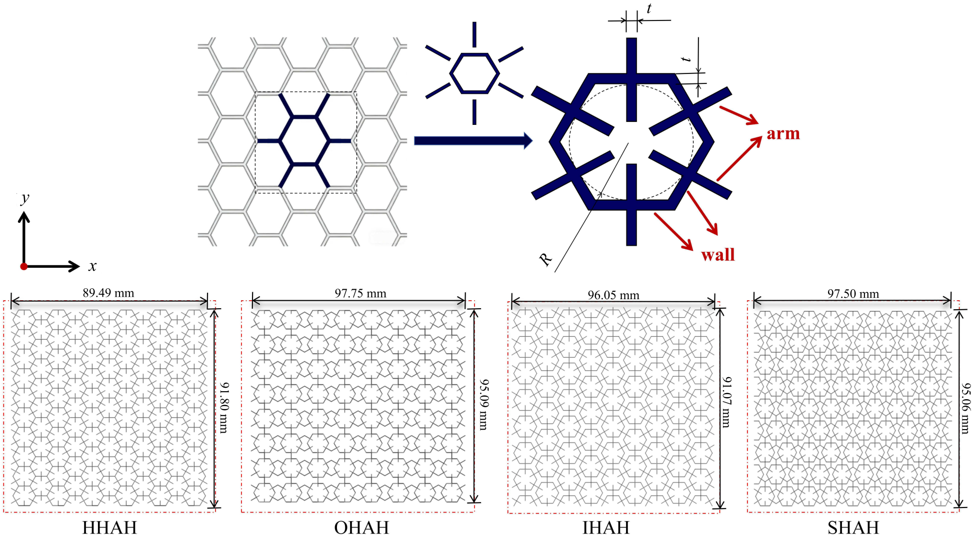

HHAH OHAH IHAH SHAH

Fig. 1. Hexa-arm honeycomb unit cell design and schematic diagram of the honeycomb structure.

Inspired by the diverse structural organizations in nature, different arrangements of unit cells were designed to optimize the load-bearing efficiency and energy absorption performance of the lattice. The specific configurations are shown in Fig. 1 and are described as follows:

(1) HHAH structure: Based on the close packing of traditional regular hexagonal honeycombs, conventional cells are replaced with hexa-arm honeycomb cells. Adjacent cells share a common wall and an arm plate, forming a highly integrated, two-dimensional periodic structure.

(2) OHAH structure: Hexa-arm honeycomb cells are arranged periodically along the x- and y-directions, forming an orthogonal lattice structure. Adjacent cells were connected via arm plates, forming an octagonal concave cavity at the connection points along the x-axis.

(3) IHAH structure: Building upon the orthogonal lattice, the even-numbered columns of the cells are shifted upward by half the cell height. This causes the top-right arm of the cell in the previous column to connect collinearly with the bottom-left arm of the cell in the subsequent column, forming a spatially continuous, inclined arrangement. Each cell was surrounded by six neighboring cells and connected via the arms.

(4) SHAH structure: Similar to the orthogonal lattice, the even-numbered rows of cells are shifted rightward by half the cell width, forming a staggered composite lattice. Unlike the inclined lattice, the arm connections between adjacent cells in this structure are not collinear but form external triangular cross-nodes. Every four cells formed a group with two opposing Y-shaped cavities at their center.

2.2. Parameters for mechanical properties

Key mechanical parameters were introduced to characterize the honeycomb material and quantitatively assess the quasi-static compressive behavior and energy absorption capacity of the structure. The nominal stress σ and strain ε of the honeycomb structure are defined as follows:

$$\sigma = \frac{F}{Lb}, \tag{2.1}$$

$$\varepsilon = \frac{\Delta H}{H}, \tag{2.2}$$

where F is the compressive force, L is the length of the honeycomb structure along the x-direction, and H is the height of the honeycomb structure along the y-direction, as shown in Fig. 1. The out-of-plane thickness b of the honeycomb structure remained constant at 10 mm, and ΔH was the impact displacement of the honeycomb structure. The plateau stress σ_p, defined as the average stress from yielding to densification during compression, is calculated as:

$$\sigma_p = \frac{1}{\varepsilon_d - \varepsilon_{cr}} \int\limits_{\varepsilon_{cr}}^{\varepsilon_d} \sigma(\varepsilon)\, d\varepsilon. \tag{2.3}$$

Here, ε_{cr} is the yield strain, $\sigma(\varepsilon)$ is the nominal stress corresponding to the strain ε, and ε_d is the densification strain. To avoid subjective bias, the densification strain was determined using the energy absorption efficiency method, expressed as

$$\sigma_p = \frac{1}{\varepsilon_d - \varepsilon_{cr}} \int\limits_{\varepsilon_{cr}}^{\varepsilon_d} \sigma(\varepsilon)\, d\varepsilon. \tag{2.4}$$

G is the energy absorption efficiency parameter of the honeycomb, which is obtained by

$$G = \frac{\int_0^{\varepsilon} \sigma(\varepsilon)\, d\varepsilon}{\sigma(\varepsilon)}. \tag{2.5}$$

The energy absorption (EA), corresponding to the area under the stress–strain curve up to the densification strain, is expressed as

$$\mathrm{EA} = \mathrm{V} \int\limits_{0}^{\varepsilon_d} \sigma(\varepsilon)\, d\varepsilon. \tag{2.6}$$

V denotes the volume of the honeycomb structure, and the specific energy absorption (SEA), defined as the energy absorbed per unit mass, is expressed as

$$\mathrm{SEA} = \frac{\mathrm{EA}}{m} = \frac{\int_0^{\varepsilon_d} \sigma(\varepsilon)\, d\varepsilon}{\bar{\rho}\rho_s}, \tag{2.7}$$

here ρ_s is the density of the base material, $\bar{\rho}$ is the relative density of the honeycomb material and can be defined as:

$$\bar{\rho} = \frac{\sum_{i=1}^{n} Rt}{LH}, \tag{2.8}$$

where n represents the total number of walls and arms of the length R in each honeycomb structure, from which the relative densities of the different honeycomb structures were calculated as 38.7% (HHAH), 37.4% (OHAH), 39.3% (IHAH), and 42.4% (SHAH), respectively.

3. Experiments and numerical simulation

3.1. Specimen preparation and material properties

All hexa-arm honeycomb structures in this study were fabricated using the Selective Laser Sintering (SLS) additive manufacturing technology. The 403P SLS system (Farsoon Technologies) was employed. The key printing parameters were as follows: laser power of 45 W, scanning speed of 10 m/s, layer thickness of 0.1 mm, and powder bed temperature of 170 °C, with a support scanning coefficient of 1.1 to compensate for the energy input in the support area and enhance the sintering strength of this region. All specimens were printed with the build direction along the out-of-lane thickness b to ensure consistent mechanical properties. No post-processing heat treatment was performed. The printing material was 7100Pro Nylon, with a density of approximately 1.07 g/cm^3 and a melting point of approximately 185.5 °C. For comparative purposes, the overall dimensions of all honeycomb specimens were controlled to be similar, as shown in Fig. 1. The fabricated specimens of each structure are shown in Fig. 2.

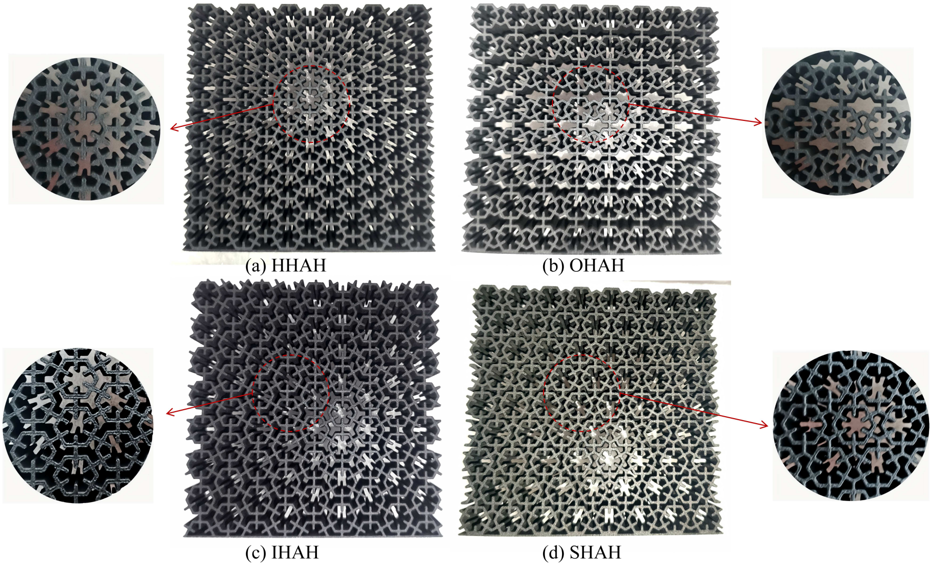
(a) HHAH
(b) OHAH
(c) IHAH
(d) SHAH

FIG. 2. Specimens of various honeycomb structures: (a) HHAH; (b) OHAH; (c) IHAH; (d) SHAH.

To determine the mechanical properties of the nylon material, standard dumbbell-shaped tensile specimens were prepared and subjected to uniaxial tensile tests at a loading rate of 1 mm/min. The uniaxial tensile tests were repeated three times on the printed specimens using serrated grips with a higher clamping pressure, and both ends of each specimen were polished with emery paper to prevent slippage. To minimize the influence of the printing direction on the mechanical properties, tensile specimens were printed along their width, ensuring that the loading direction was aligned with the tension and compression directions of the cells in the honeycomb structures. The stress-strain curve obtained from the tensile test is shown in Fig. 3, indicating an initial linear elastic behavior followed by a distinct plastic deformation stage, exhibiting typical elastoplastic characteristics.

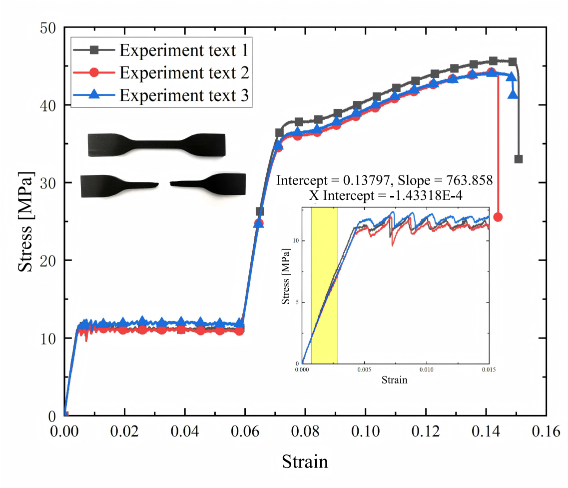

Fig. 3. Engineering stress-strain curves of the 7100Pro Nylon material from uniaxial tensile tests.

The key mechanical parameters of the material were extracted from the stress-strain curve and are summarized in Table 1. The following methods were used to determine the key mechanical parameters from the engineering stress–strain curve: the elastic modulus was calculated from the slope of the linear elastic region between strains of 0.0005 and 0.0025. The yield stress was determined using the 0.2% offset method: a line parallel to the initial elastic slope was drawn from the 0.2% strain, and its intersection with the stress–strain curve defined the yield stress. The failure strain was recorded as the strain at which complete fracture occurred. These parameters were used as material property inputs for the subsequent finite element modeling.

Table 1. Material properties.

ρ [$\mathrm{g} \cdot \mathrm{cm}^{-3}$]	E [MPa]	μ	σ_y [MPa]	σ_u [MPa]
1.07	763.86	0.3	10	45

3.2. Quasi-static in-plane compression tests

To evaluate the mechanical performance and energy absorption capacity of the honeycomb structures, quasi-static in-plane compression tests were conducted using the DDL300 universal testing machine equipped with a 20 kN load cell, as shown in Fig. 4. The test was conducted in the displacement control mode, and the specimen was positioned at the center of the lower platen. The upper platen descended at a constant rate of 3 mm/min until the specimen reached an 80% strain in the y-direction. Throughout the process, the testing machine automatically recorded the load, displacement, and time. The nominal stress σ and strain ε were calculated using the formulas provided in Subsection 2.2, respectively. The entire compression process was documented using video recording.

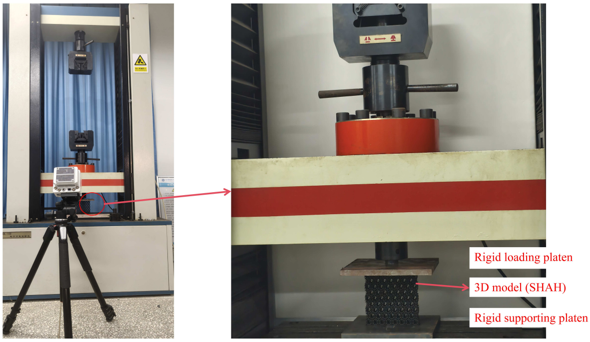

Fig. 4. Quasi-static compression test setup.

Three identical specimens were fabricated for each honeycomb configuration and tested under identical loading conditions. The reported stress-strain curves are the averages of three repeats, and the corresponding standard deviations are shown as error bands in Section 4.

3.3. Numerical simulation

The finite element software ABAQUS was employed to simulate the in-plane uniaxial compression process of different honeycomb structures. The quasi-static compression was simulated using an explicit dynamics solver (ABAQUS/Explicit). To ensure a quasi-static response, the loading rate was artificially increased, and the kinetic energy of the model was monitored throughout the analysis, maintaining it below 5% of the internal energy to minimize the inertial effects. As shown in Fig. 5, the numerical model consisted of three parts: a movable rigid platen, a fixed rigid platen, and a honeycomb specimen sandwiched between them.

The honeycomb structures were modeled using an elastoplastic constitutive model. They were meshed with S4R elements (4-node linear brick, reduced integration) and an hourglass control to suppress the zero-energy modes. The material parameters were determined based on the uniaxial tensile test stress-strain curve shown in Fig. 3, with the specific values listed in Table 1. The exclusion of fracture and damage mechanics is justified for the primary focus of this study, which is on the energy absorption mechanisms during the elastic

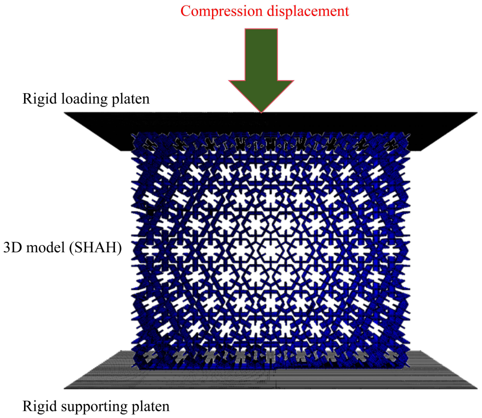

Fig. 5. Numerical simulation model of the SHAH.

and plateau stages, where buckling and the plastic hinge formation are the dominant energy dissipation modes. This simplification is commonly adopted in numerical studies of ductile honeycomb crushing [58–60]. Additionally, the simulation model employs a shell element model, which generates lower nominal stresses compared to solid models during quasi-static compression simulations. To reduce the computational resource consumption and enhance the simulation efficiency, this study intentionally omitted the material fracture behavior from the analyses. The interfacial contact between the structural components was defined using the extended Lagrange algorithm. Nevertheless, ignoring fractures may lead to a slight overestimation of the SEA in the very late stages of densification (beyond approximately 65% strain), where material tearing could occur in physical tests. Future studies should incorporate damage initiation and evolution criteria to address this limitation.

The von Mises yield criterion and isotropic hardening model were adopted in this study. The rigid platens were modeled as discrete rigid bodies. The normal contact behavior between the platens and honeycomb structure was defined using a pressure-overclosure relationship, which strictly minimized penetration between the surfaces. Tangential contact was modeled using a penalty friction formulation with a friction coefficient of 0.3 (see Subsection 3.5 for a detailed discussion of friction). The bottom platen was then fixed. The top platen was constrained to allow movement only in the y-direction (compression direction) and was subjected to a downward displacement load, compressing the structure to 80% of its initial height.

A mesh sensitivity analysis was conducted using the SHAH structure as an example, employing mesh sizes of 5, 3, and 1 mm. The resulting load-displacement curves are shown in Fig. 6. The differences between the results for the

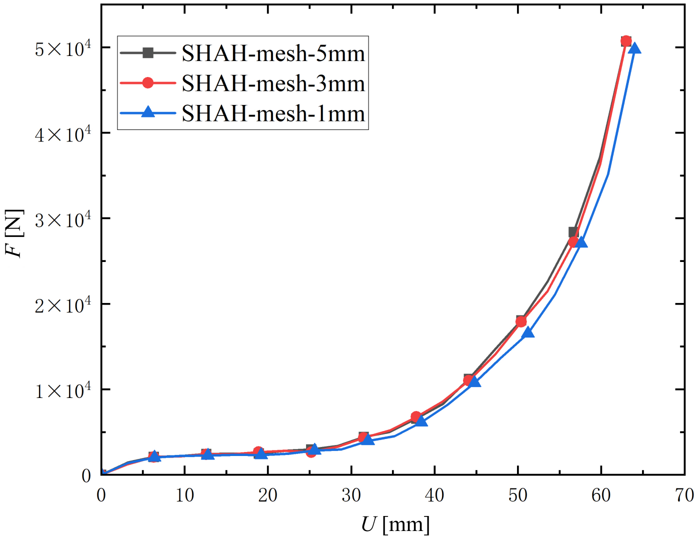

Fig. 6. Load-displacement curves for SHAH structure with different mesh sizes.

three mesh sizes were less than 5%, indicating an acceptable mesh influence and satisfying the mesh independence requirements of the study. Consequently, a mesh size of 1 mm was adopted for all subsequent simulations.

3.4. Validation of the constitutive model

To validate the elastoplastic material model used in the honeycomb simulations, a finite element model of a standard dumbbell-shaped tensile specimen was created. The same material parameters (Table 1) and von Mises yield criterion with isotropic hardening were employed. The tensile test was simulated under displacement control at 1 mm/min to match the experimental loading rates. Because the current material model does not include a fracture criterion, the simulation was limited to the elastic and early plastic regimes (up to a strain of approximately 0.05 only).

The simulated engineering stress-strain curve was compared with the experimental curve from the repeated tensile test, as shown in Fig. 7. The simulated curve matches the experimental curve reasonably well in terms of the elastic modulus, yield stress, and initial hardening slope, although a small discrepancy in the initial slope is observed. The small deviation in the initial slope may arise from the inherent viscoelastic nature of the laser-sintered nylon material, which is not captured by the purely elastoplastic model employed in this study, as well as from the simplified clamping conditions in the tensile test simulation.

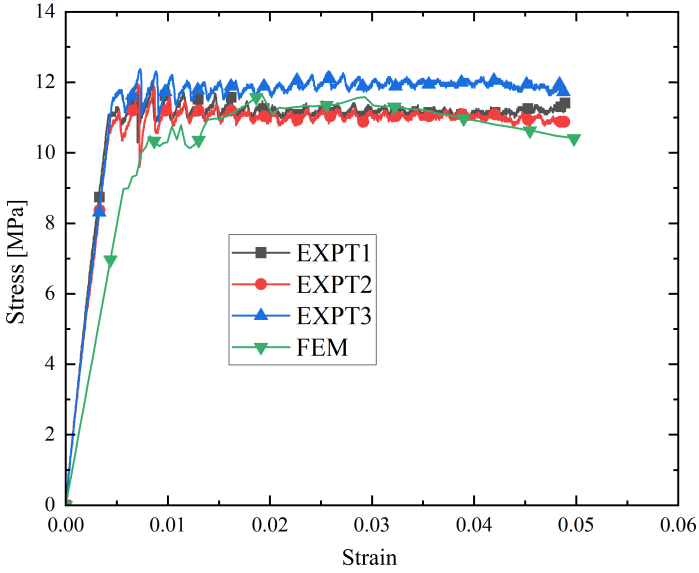

FIG. 7. Validation of the elastoplastic constitutive model.

Despite this minor difference, the finite element model reproduces the overall experimental behavior very well in the subsequent stages, as demonstrated by the good agreement in the full-scale honeycomb compression simulations presented in Subsections 4.2 and 4.4. Therefore, the constitutive model is considered adequate for the purpose of this study.

3.5. Effect of friction coefficient

The friction coefficient between the honeycomb specimen and rigid platens was set to 0.3 in the main simulations, based on typical dry friction values for nylon–steel interfaces (ranging from 0.2 to 0.4). To evaluate the sensitivity of the numerical results to this parameter, a series of simulations were performed on the SHAH structure using friction coefficients of 0.1, 0.3, and 0.5.

Figure 8 shows the stress-strain curves obtained using different friction coefficients. The initial peak stress showed minor variations (less than 5%) across the three values. More importantly, the plateau stress, densification strain, and the overall deformation mode were almost identical, indicating that the friction coefficient had a negligible effect on the energy absorption performance under the current loading conditions. This insensitivity is attributed to the fact that the dominant deformation mechanisms – cell wall buckling, the contact between arms, and the plastic hinge formation – occur within the structure, whereas relative sliding at the platen interfaces is limited.

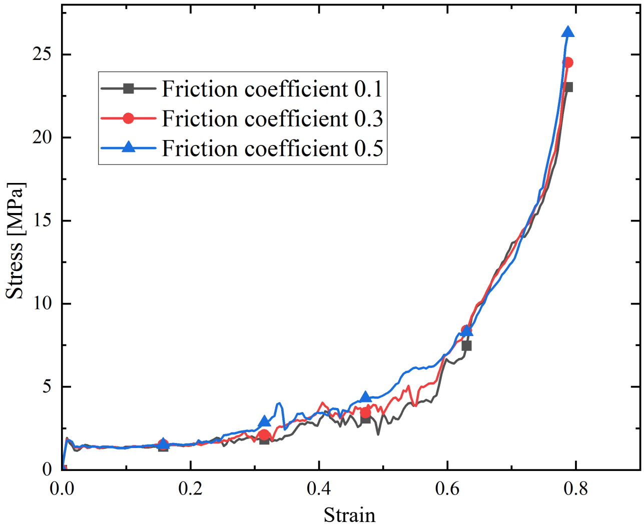

Fig. 8. Stress-strain curves of the SHAH structure obtained with different friction coefficients.

Based on this sensitivity study, a friction coefficient of 0.3 was considered appropriate and used in all subsequent simulations. The observed low sensitivity is consistent with the findings in the literature [61], which reported that friction plays a secondary role in honeycomb in-plane compression when the deformation is dominated by internal buckling.

4. Results analysis and discussion

This section presents and analyzes the experimental and numerical simulation results for various cellular metamaterials subjected to in-plane compressive loading. The reliability of the finite element model was first validated by comparing the deformation patterns with the stress-strain curves. Subsequently, it focuses on contrasting the in-plane compressive performance and energy absorption characteristics of different structures.

4.1. Deformation analysis of compression process

Through a comparative analysis of the experimental and simulation results, this section elucidates the underlying mechanism linking the structural configuration and mechanical properties of the hexa-arm honeycomb. The markedly distinct deformation patterns exhibited by various structures during compression demonstrate the fundamental difference in the mechanical response between the different hexa-arm honeycomb structures.

Figure 9 shows the quasi-static compression test and simulated deformation process of the HHAH structure. According to the Mises stress distribution from the finite element simulations, the deformation of this structure was relatively uniform during compression, without significant local stress concentrations or localized failure. The diagram reveals that during the initial deformation phase, the HHAH structure underwent deformation primarily on the sides. As the unit cell is compressed, its deformation causes the sidewall panels to gradually come into contact. This interaction transfers the vertically downward compressive force toward the panel-facing side, thereby altering the primary load-transfer path. Consequently, the structure began to bend unilaterally, modifying the deformation morphology of the honeycomb structure. As the deformation increased, the structure of the unit cells changed, thereby altering the force transmission path of the arm. The horizontal force increased, leading to deformation on both sides of the structure. As the compressive strain increased, the structure progressively collapsed in the horizontal direction, and the overall structure underwent significant deformation.

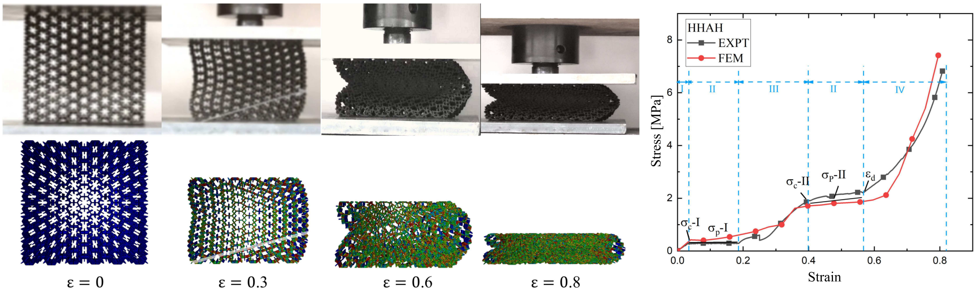

Fig. 9. Deformation process of HHAH structure.

Under sustained compressive loading, the structure collapsed sequentially, exhibiting noticeable lateral buckling. Eventually, the hexa-arm honeycomb cells were nearly completely disintegrated, and the nominal stress increased rapidly.

Figure 10 shows the quasi-static compression test and the corresponding simulated deformation process of the OHAH structure. The von Mises stress distribution from the finite element simulations indicated that this structure initially exhibited bending deformation in local inverted triangular regions, with a relatively uneven stress distribution. The deformation diagram reveals that, owing to its unique structural configuration, the wall panels between adjacent cells uniformly distributed vertical downward compressive forces outward. This results in relatively uniform structural deformation, with each cell fully utilizing its functional capability. The analysis primarily focused on the connections

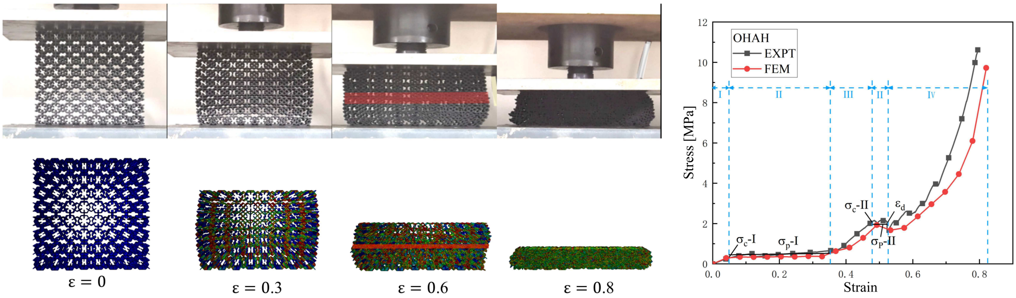

Fig. 10. Deformation process of OHAH structure.

between the arms, indicating that they bore a greater load during the initial stages of deformation. This arrangement alters the stress transmission path within the structure, resulting in stress concentrations in specific areas. Furthermore, the deformation of the honeycomb unit cells was slightly less than that of the previous two structures.

As the compressive strain increased (to approximately 0.45 equivalent strain), the stress distribution gradually homogenized through the coordinated deformation of the internal cells, entering the stage of overall uniform compression without a significant crack formation. The honeycomb cell layers failed successively until the structure was fully densified.

Figure 11 shows the quasi-static compression test and the simulated deformation process of the IHAH structure. According to the von Mises stress distribution obtained from the finite element simulations, the deformation was relatively uniform in the initial stage of compression. In the elastic stage, loads were primarily transmitted through the connecting arms between the honeycomb cells, causing a slight lateral expansion of the overall structure and early local failure, with initial cracks forming along the shear band direction of the

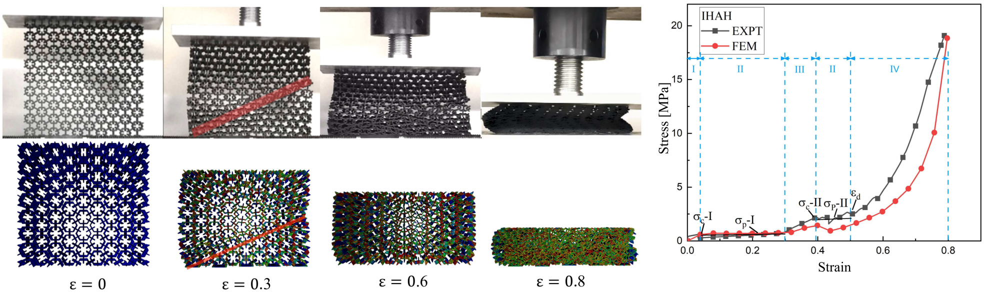

Fig. 11. Deformation process of IHAH structure.

structure. This may be attributed to the unique connection method of the structure, where the unit cells are arranged in an inclined manner, transmitting vertical downward pressure along the arms in the direction of shear. The layout adopts an inclined arrangement, with individual cells connected by the panel walls. Under compressive stress, these wall panels deform first. Owing to the inclined connection of the wall panels, the structure bent toward one side during deformation. In addition, the arm plates effectively resisted external stress through bending deformation, which played a crucial role in supporting the structure. As compression continued, significant failure occurred along the shear band direction of the specimen.

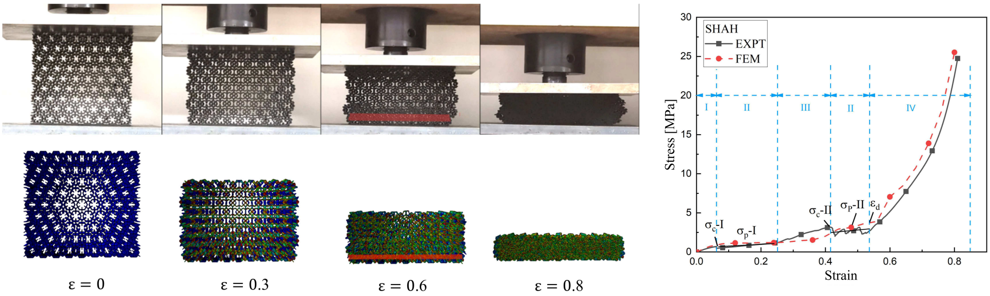

Fig. 12. Deformation process of SHAH structure.

Figure 12 shows the quasi-static compression test and the corresponding simulated deformation process of the SHAH structure. The von Mises stress distribution from the finite element simulations showed that this structure deformed uniformly during compression, with a relatively continuous stress distribution. The load applied from the top was transmitted downward through the nodes. In the SHAH structure, adjacent unit cells are staggered in arrangement, with their interconnected wall panels forming a Y-shaped configuration. This design enhances the ability of the structure to withstand downward compressive forces while dispersing them outward, resulting in a more uniform stress distribution across the entire framework. Simultaneously, because the nodes are connected to the left and right adjacent cells, part of the compressive force is transformed into tensile stress in the horizontal direction, subjecting the entire structure to a lateral tension. The shape of the honeycomb cells changed: the nodal regions were compressed, their connection forms gradually transitioned from the original triangular configuration to a rectangular one. As the shape of the honeycomb cells changes, the wall panels also adapt accordingly. The interactions and collisions between different wall panels form distinct platforms, resulting in a more uniform and hierarchical structural morphology under compressive forces.

Unlike conventional honeycomb structures, the SHAH structure undergoes a cell shape change in the initial deformation stage but does not exhibit compressive failure at this stage. As deformation progressed, horizontal cracks appeared. Owing to the influence of the stress transmission path, the bottom region failed first. With a continued increase in the in-plane compressive strain, the second layer of the structure collapsed sequentially, the lower part gradually densified, the upper part continued to fail under pressure, and a second horizontal crack formed almost simultaneously at the interface between the upper and lower layers. The SHAH structure enhances the connection and stress transmission through the external Y-shaped arms, which transform into I-shaped arms during compression. This configuration effectively distributed the load across the honeycomb, resulting in a relatively uniform stress distribution throughout the compression.

Finally, the interlocking honeycomb cells completely disintegrated, and the structure entered the densification stage. At this stage, the nominal stress increased rapidly, and the overall deformation mode transitioned to a response dominated by the lateral bending of the beam.

From Figs. 9–12, it can be observed that the compression process of the hexa-arm honeycomb generally can be divided into four stages: linear elastic stage (I), plateau stage (II), second linear elastic stage (III), and densification stage (IV). The plateau stage (II) included a relatively stable stress response between the two elastic stages. Similar stage divisions have been reported in other studies on the modified honeycomb structures. Notably, the plateau stage (II) of the hexa-arm honeycomb was significantly shorter than that of the conventional honeycomb. Taking the SHAH structure as an example, the plateau stage after the first elastic stage was not distinct, and transitioned almost directly into the second elastic stage, where the stress level was relatively close to that of the first elastic stage. This was followed by a more pronounced plateau segment acting as a buffer, which was clearly captured in the finite element simulations and agreed well with the experimental results. Furthermore, all hexa-arm structures exhibited higher stress levels in the second elastic stage (stage III). After the second elastic stage, the stress decreased slightly and remained stable for a certain duration. With further compression, the stress increased rapidly when entering the densification stage.

The secondary linear elastic phase (stage III) is a geometric effect caused by the contact and interlocking of the hexa-arms, rather than an intrinsic material property of nylon. The uniaxial tensile curve of the nylon material (Fig. 3) shows a smooth elastic plastic – transition with no secondary linear elastic region, excluding the material origin.

To further elucidate this mechanism, the local deformation of the SHAH unit cell was analyzed, as shown in Fig. 13. Under compressive stress, the upper

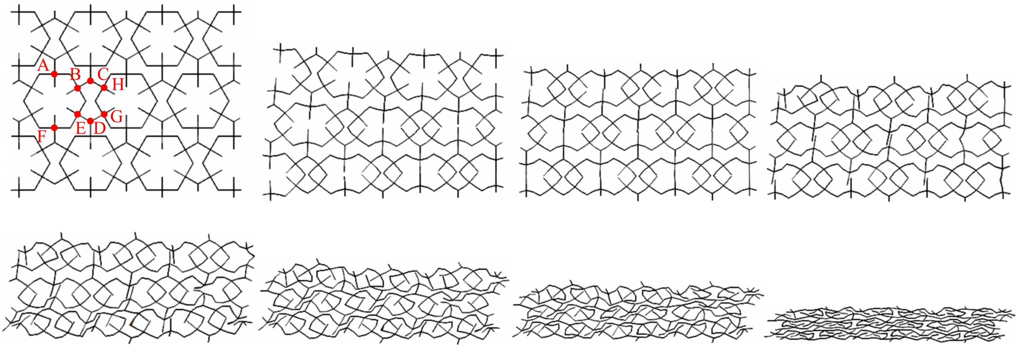

Fig. 13. Local deformation process of the SHAH structure.

and lower sides of the SHAH unit cell caved inwards. Owing to the periodic arrangement, the movement direction of each unit cell was consistent at the initial compression stage, allowing the cells to coordinate the bending deformation through concave deformation. As the unit cells cave in, the walls contact each other. Specifically, the walls containing points C and D formed a new rhombic structure, and the honeycomb edges at points B, D, H, and G formed new wall structures. This contact created additional load paths, temporarily stiffened the structure, and manifested as a second linear elastic increase in the stress-strain curve (sage III). The Y-shaped cavities in the SHAH structure promote early contact with the arm. Consequently, the newly formed walls optimize the concave angles, reduce the stress concentration, and improve the load transfer and structural stiffness, thereby enhancing the overall stability and reliability of the SHAH configuration.

These phenomena demonstrate that the mechanical response of a structure can be effectively regulated by incorporating additional arms within the cells or modifying their connection methods. During compression, most hexa-arm honeycombs exhibited densification behavior in the node regions that progressively developed from the high-density top zone to the low-density bottom zone, ultimately achieving complete densification. Owing to the asynchronous densification processes in the upper and lower sections, the structure frequently adopts a laterally bending configuration during deformation. For the hexa-arm honeycomb, the stress was primarily concentrated in the arm plate regions from the elastic stage to densification. The numerical simulations and experimental results were generally consistent, although some deviations occurred during the elastic failure stage, which could be attributed to internal defects in the 3D-printed material. In contrast, for a conventional honeycomb structure under compressive failure, the stress is mainly concentrated along the shear band direction, and the structure collapses layer by layer, with the collapse angle relative to the platform gradually decreasing until full densification is achieved. Among the hexa-arm structures, the IHAH structure initially collapsed along an inclined direction. However, as deformation developed, the collapse angle gradually decreased and eventually became horizontal. The other hexa-arm structures only underwent cell shape changes without significant collapse in the early stage of deformation, exhibiting horizontal collapse only after the deformation exceeded a certain degree. The experimental and simulation results confirmed that the failure modes of the hexa-arm honeycomb structures were closely related to their arrangement patterns.

4.2. Compressive performance

The error band analysis (Fig. 14) shows that the repeated tests for each honeycomb configuration yielded nearly identical stress–strain responses, with the shaded standard deviation bands remaining narrow across the entire strain range. This indicates the excellent repeatability of the experimental data. The

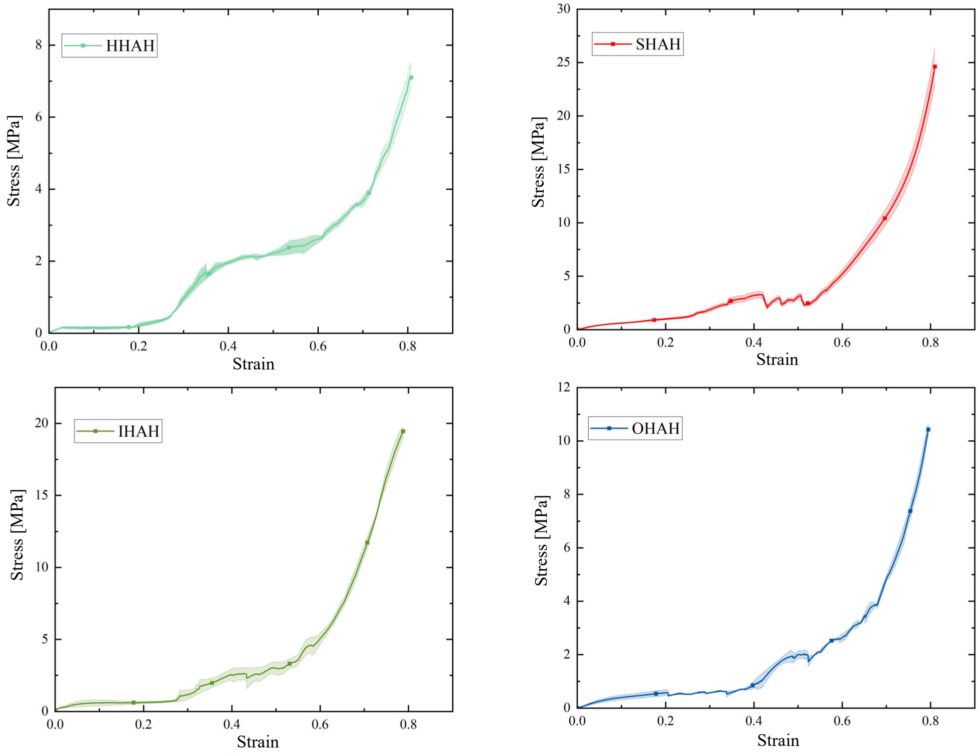

Fig. 14. Experimental stress-strain curves (solid line: average of three repeats; shaded band: ± one standard deviation, $n = 3$) of the four structures.

maximum coefficient of variation among the three repeats for any configuration was below 5%, confirming that the 3D-printed specimens and test setup produced highly consistent results.

Figure 15 compares the experimental and simulated mechanical properties of the four hexa-arm honeycomb structures, including the elastic modulus (E), peak stress (σ_c), plateau stress (σ_p), and densification strain (ε_d). Figure 15(a) shows the elastic moduli of different structures during the elastic stage, where the locally stiffened honeycomb structure exhibited different elastic moduli in elastic stages I and III. All hexa-arm structures exhibit a higher elastic modulus in stage II than in stage I, with the OHAH structure showing the most pronounced increase, whereas the two-stage moduli of the SHAH structure are relatively close together. Figure 15(b) shows the peak stress (σ_c), which marks the onset of significant plastic deformation and serves as the effective peak stress

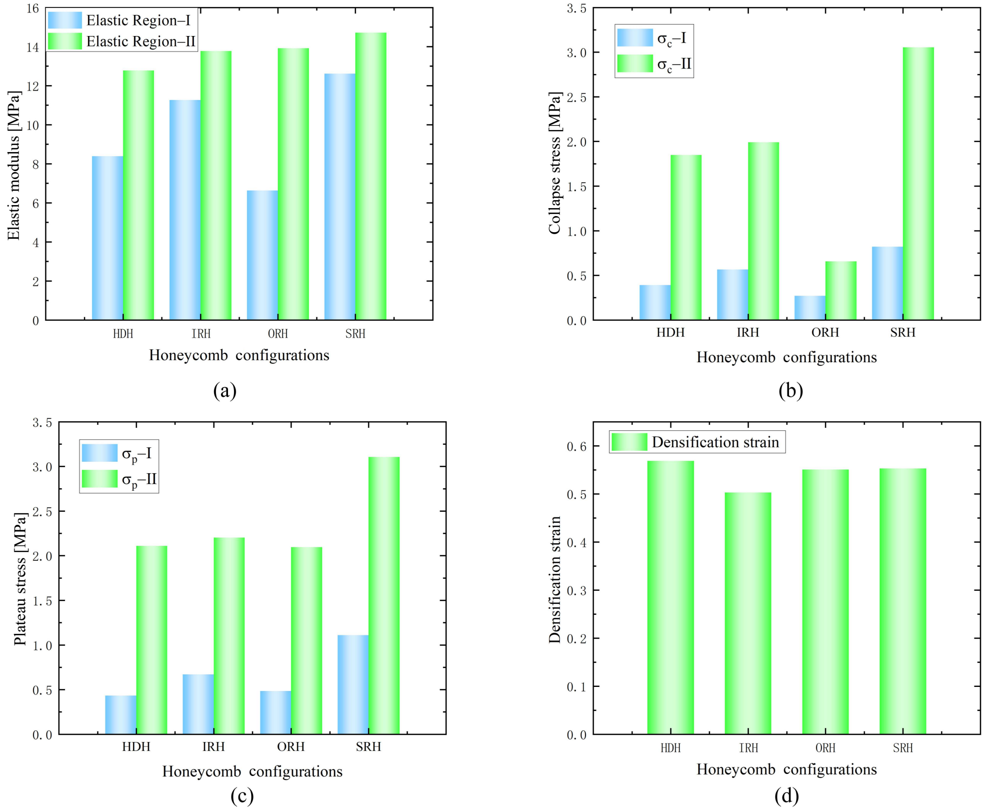

(a) (b) (c) (d)

FIG. 15. Mechanical properties of hexa-arm honeycombs under in-plane compression: (a) elastic modulus (stage I & II); (b) peak stress (σ_c, stage I & II); (c) plateau stress (σ_p, stage I & II); (d) densification strain (ε_d).

for these structures owing to the smooth elastic plateau transition. All hexa-arm structures showed a multiple-fold increase in peak stress from stage I to stage II, indicating their sensitivity to the structural morphology. Figure 15(c) shows the plateau stress (σ_p), defined by Eq. (2.3), as the average stress from yielding to the densification. Although the second plateau stage is very short, its plateau stress σ_p-II is approximately 3–4 times higher than σ_p-I, with some dependence on the structural configuration of the specimen. Figure 15(d) compares the densification strain (ε_d). All the structures were densified at strains of approximately 0.5, showing little correlation with the arrangement pattern.

Figure 16 shows the stress-strain response of different honeycomb structures under in-plane compressive loading, comparing the deformation behaviors of different hexa-arm structures. It can be seen that the stresses of all the hexa-arm structures were quite excellent. Specifically, four stages were observed for hexa-arm honeycombs. The stress in the initial stage did not differ significantly, possibly because the deformation was small and the arm support was not fully mobilized. Upon entering the second stage, the structures exhibited a more pronounced and stable high-plateau response, reflecting the unique deformation resistance mechanism of the hexa-arm honeycomb. In addition, the nominal stress exhibited a significant increase after the second elastic stage. Throughout the compression process, the deformations of the different hexa-arm structures varied considerably. The SHAH structure exhibited the best stress performance, followed by the IHAH one. Although the stresses of the HHAH and OHAH structures also increased substantially after the second elastic stage, the magnitude of the increase was smaller than that of the SHAH and IHAH structures. The load-bearing performance of hexa-arm honeycombs with different arrangement

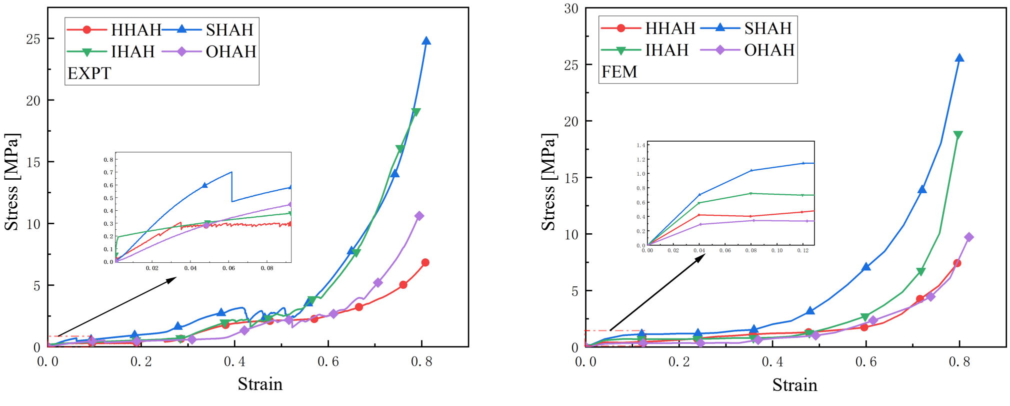

(a)

(b)

Fig. 16. Stress-strain curves of hexa-arm honeycombs: (a) experimental data; (b) simulation data.

patterns under large deformation compression varies, demonstrating a dependence on the structural configuration.

4.3. Poisson's ratio

In the mechanical property analysis of honeycomb structures, Poisson's ratio serves as a critical parameter for evaluating lateral deformation under tensile and compressive loads. Poisson's ratio μ is defined as the ratio of longitudinal strain to lateral strain during tensile or compressive processes, and is expressed by the following formulas:

$$\Delta\bar{L} = \frac{1}{n}\sum_{i=1}^{n}(L_{p_{ri}} - L_{p_{li}}) \qquad (i = 1, 2, \ldots, n), \tag{4.1}$$

$$\Delta y = \frac{\Delta y_r + \Delta y_l}{2} = \frac{(y_{r1} - y_{rn}) + (y_{l2} - y_{ln})}{2}, \tag{4.2}$$

$$\Delta y = \frac{\Delta y_r + \Delta y_l}{2} = \frac{(y_{r1} - y_{rn}) + (y_{l2} - y_{ln})}{2}. \tag{4.3}$$

As shown in Fig. 17, $L_{p_{ri}}$ and $L_{p_{li}}$ denote the horizontal coordinates of points p_{ri} and p_{li}, while y_{r1}, y_{rn}, y_{l2}, and y_{ln} represent the vertical displacements at points p_{r1}, p_{rn}, p_{l1}, and p_{ln}, respectively.

Figure 17 illustrates dynamic Poisson's ratio variations of the four studied structures under large deformation compression. The figure clearly shows that all the structures exhibit positive values of Poisson's ratio. Dynamic Poisson's ratio trends were similar across the structures, with a rapid initial increase during compression, reaching peak values between 0.06 and 0.08 strain, followed by a sharp decline. After 0.2 strain, Poisson's ratio continued to decrease but at a much slower rate.

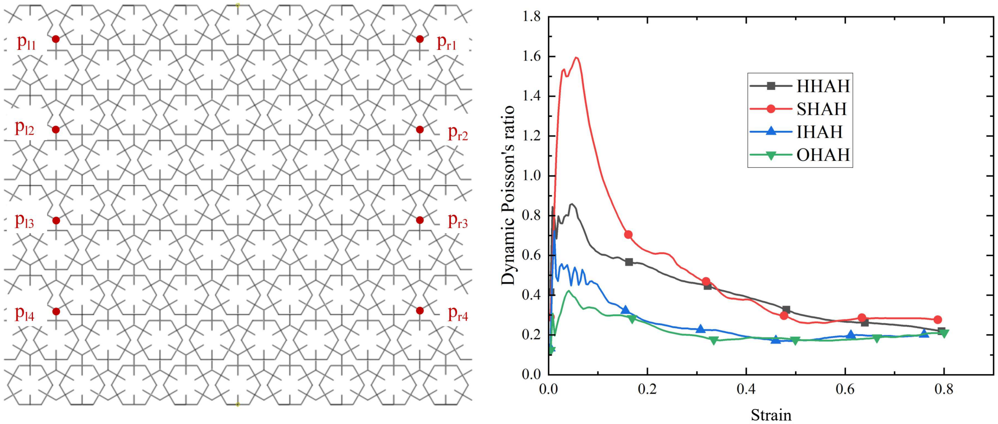

FIG. 17. Dynamic Poisson's ratio of the four hexa-arm honeycomb structures.

Although the four structures shared comparable Poisson's ratio trends, their numerical values differed notably. Before a strain of 0.4, the SHAH configuration exhibited the highest Poisson's ratio among the four structures, followed by the HHAH. The IHAH configuration exhibited slightly higher Poisson's ratio than the OHAH configuration before a strain of 0.2. Beyond a strain of 0.2, Poisson's ratios of the OHAH and other structures exhibited minimal variation. The analysis of dynamic Poisson's ratios revealed that the structural arrangement significantly influenced Poisson's ratio behavior.

4.4. Energy absorption

Figure 18 demonstrates the influence of structural configurations on energy absorption performance under in-plane compression conditions for various hexa-arm honeycomb structures, along with a comparative analysis of experimental and simulation results regarding energy absorption capacity.

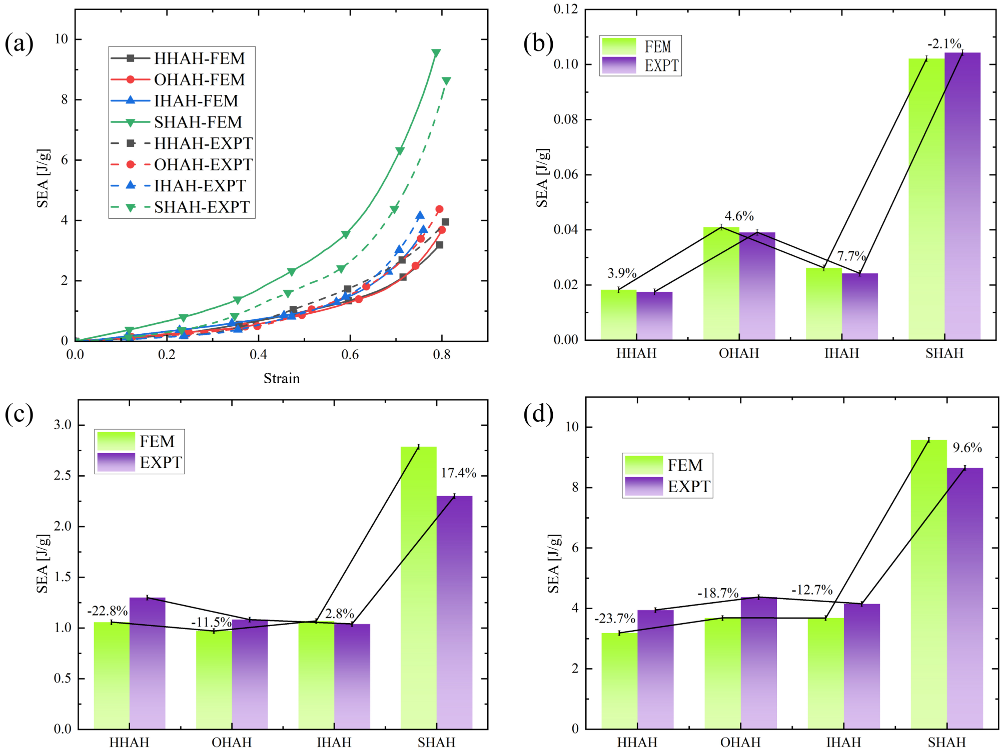

Fig. 18. Energy absorption of hexa-arm honeycombs: Comparison of SEA between experiments and simulations. (a) Overall SEA up to densification; (b) SEA at $\varepsilon \approx 0.05$ (end of first elastic stage); (c) SEA at $\varepsilon \approx 0.55$ (onset of densification); (d) SEA at densification completion ($\varepsilon \approx 0.80$).

Figure 18(a) presents a comparative analysis of the experimental and simulation results for hexa-arm honeycomb structures with different configurations under quasi-static compression using the SEA method. The figures demonstrate that the simulation and experimental SEA values show minimal overall discrepancies, with only the SHAH structure exhibiting significantly lower experimental SEA values than those of the simulations. This discrepancy may stem from the fact that the simulation models did not account for fracture damage, whereas the SHAH structures possessed the highest relative density among the four configurations, leading to more pronounced fracture-damage effects. Nevertheless, the overall structural alignment remains consistent. Figure 18(b) compares the SEA values at approximately 0.05 strain (during the completion of the initial elastic phase). The results indicate that the SHAH structures continue to demonstrate superior energy absorption performance compared to the other configurations during the initial stage, with negligible differences between the simulation and experimental data, thus confirming good initial phase alignment. Figure 18(c) shows SEA comparisons at 0.55 strain (when approaching the densification phase initiation). While the SEA values for SHAH and the three other structures showed negligible differences, the simulation results for the HHAH and OHAH structures consistently underperformed the experimental measurements. This discrepancy may arise from shell element modeling techniques that delay the edge contact interaction compared with physical models during compression. Figure 18(d) shows the SEA comparison at the completion of the densification phase (compression termination). Although the experimental and simulation results exhibited minor deviations, these errors remained within acceptable tolerance ranges, thereby validating the reliability of the simulation results.

The overall results shown in Fig. 18(a) demonstrate that the SHAH structure exhibits a significantly higher energy absorption performance than the other structural configurations. Although the remaining structures exhibited comparable energy absorption capabilities, their growth processes differed, with distinct optimal-absorption phases. All configurations demonstrated substantial growth after entering the densification stage. In conclusion, the hexa-arm structure significantly enhanced the energy absorption capacity of the structure, and this capacity was closely related to its structural configuration.

4.5. Comparison with conventional hexagonal honeycomb

To quantify the mechanical advantage of the hexa-arm design, a conventional regular hexagonal honeycomb was designed with a circumscribed circle radius ($R = 4$ mm), the same wall thickness ($t = 1.0$ mm), and the same base material (7100Pro Nylon) identical to those of the four structures investigated in this study. For the numerical simulations, a validated finite element model was employed to simulate the conventional honeycomb under the same quasi-static compression conditions (including the loading rate, boundary conditions, and the friction coefficient).

Figure 19 compares the nominal stress–strain curves and the SEA at key strain points for the conventional honeycomb and SHAH structures under quasi-static in-plane-compression. The SHAH structure exhibited stress levels similar to those of the conventional honeycomb during the initial deformation phase (before the strain reached 0.05), likely because the deformation was small and the arms had not yet begun to function. As the strain increased, the SHAH structure demonstrated a significantly superior nominal stress performance compared with the conventional honeycomb. During the second plateau stage, the plateau stress of the SHAH structure exceeded that of the conventional honeycomb by 659.8%, and its SEA was 111.3% higher. As the densification phase approached, the SEA of the SHAH structure surpassed that of the conventional honeycomb by 155.1%. This performance enhancement is primarily attributed to the newly introduced load-bearing-arm structure and staggered arrangement pattern, which effectively delayed local structural collapse and achieved a more uniform stress distribution.

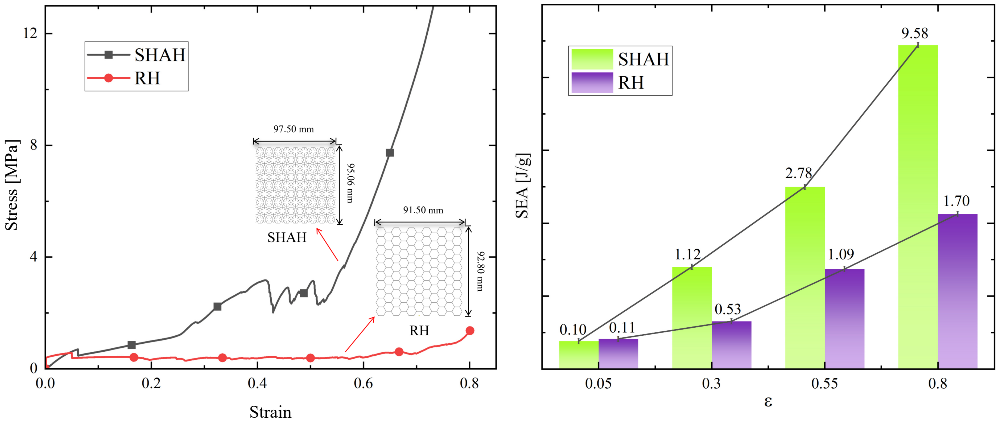

Fig. 19. Comparison of mechanical properties between SHAH and RH.

These results quantitatively demonstrate that the hexa-arm topology, particularly the SHAH configuration, provides a substantial enhancement in the energy absorption performance compared to the conventional design at the same relative density.

5. Parametric analysis of the influence on mechanical performance

5.1. Effect of the wall thickness t

This section focuses on comparing and analyzing the load-bearing performances of the four honeycomb structures with different arrangements and varying wall thicknesses. The radius of the inscribed circle of the honeycomb was uniformly set to $R = 4$ mm, with a wall thicknesses of 0.6, 0.8, 1.0, and 1.2 mm. The stress-strain curves for different wall thicknesses are shown in Fig. 20. The load-bearing capacity of all honeycomb types increased with wall thickness, primarily because of the increase in the material volume as the wall thickness increased. Notably, within the strain range of 0.50–0.65, OHAH and SHAH exhibited a distinct second plateau stage, after which the honeycomb structures entered the densification stage at a strain of approximately 0.70.

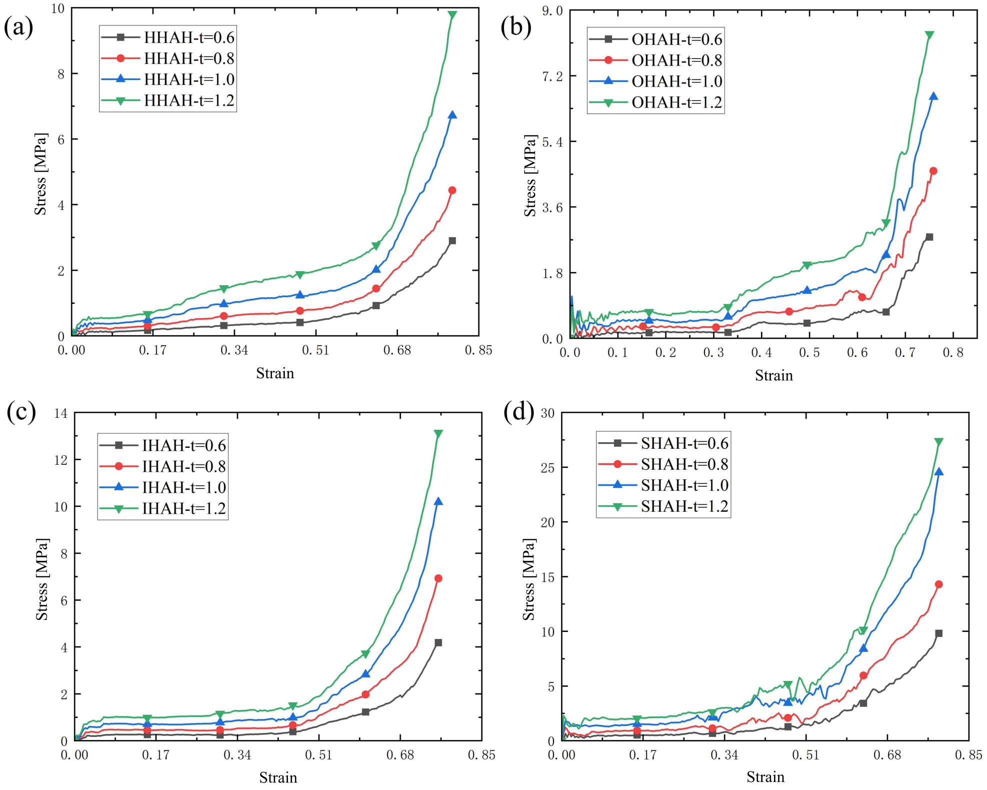

Fig. 20. Stress-strain curves with different wall thicknesses: (a) HHAH, (b) OHAH, (c) IHAH, (d) SHAH.

Figure 21 illustrates the SEA for different wall thicknesses, with the specific numerical values provided in Table 2. As shown in Fig. 21, the SEA values of all

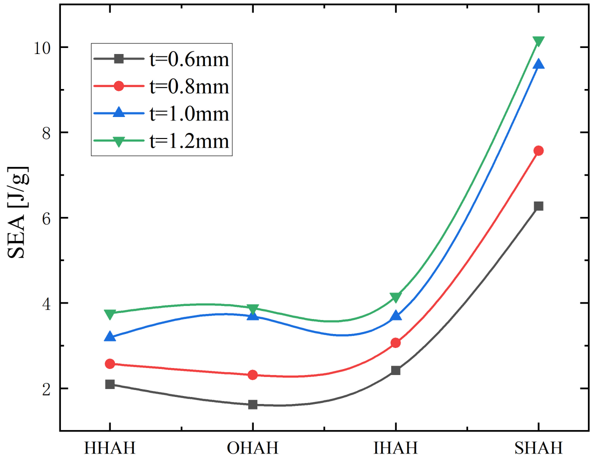

Fig. 21. SEA with different wall thicknesses.

honeycombs increased with wall thickness. When the wall thickness increased from 0.6 to 1.2 mm, the SEA of HHAH, OHAH, IHAH, and SHAH increased by 179.6%, 190.5%, 171.9%, and 162.1%, respectively. Overall, increasing the wall thickness significantly enhanced the energy absorption performance of the honeycomb specimens.

Table 2. Parameters and SEA values of the four types of honeycombs with different wall thicknesses.

Honeycombs	R [mm]	t [mm]	$\bar{\rho}$	SEA [J/g]
HHAH	4	0.6	0.232	2.093
OHAH	4	0.6	0.224	1.617
IHAH	4	0.6	0.236	2.416
SHAH	4	0.6	0.254	6.271
HHAH	4	0.8	0.310	2.573
OHAH	4	0.8	0.299	2.314
IHAH	4	0.8	0.314	3.063
SHAH	4	0.8	0.339	7.567
HHAH	4	1.0	0.387	3.190
OHAH	4	1.0	0.374	3.685
IHAH	4	1.0	0.393	3.682
SHAH	4	1.0	0.424	9.582
HHAH	4	1.2	0.464	3.759
OHAH	4	1.2	0.449	3.081
IHAH	4	1.2	0.472	4.153
SHAH	4	1.2	0.509	10.165

Although the SEA generally increases with relative density, the improvement is strongly topology-dependent. For example, at similar relative densities ($\bar{\rho} \approx 0.23$–0.25), the SHAH structure achieved an SEA of 6.27 J/g, which is approximately 2.6–3.9 times higher than those of the HHAH (2.09 J/g), OHAH (1.62 J/g), and IHAH (2.42 J/g) structures. At a higher relative density range ($\bar{\rho} \approx 0.31$–0.34), SHAH still shows an SEA of 7.57 J/g, compared to 2.57–3.06 J/g for the other three topologies. This demonstrates that the staggered arrangement pattern (SHAH) provides a topology-dependent advantage that is not merely a consequence of the increased relative density.

5.2. Effect of circle radius R

This section primarily analyzes the influence of the inscribed circle radius R on the mechanical behavior of honeycomb structures with different arrangements while maintaining a constant wall thickness across all structures ($t = 1$ mm). The specific parameters are listed in Table 3. Figure 22 shows the stress-strain curves of the honeycomb structures under compressive loading. It can be observed that when $R = 3$ mm, the strain of all honeycomb structures was significantly higher than that in the other cases. This phenomenon may be attributed to the excessively high relative density of the honeycomb structure at this radius,

Table 3. Parameters and SEA values of the four types of honeycombs with different cylindrical radii.

Honeycombs	R [mm]	t [mm]	$\bar{\rho}$	SEA [J/g]
HHAH	3	1.0	0.516	10.568
OHAH	3	1.0	0.252	10.029
IHAH	3	1.0	0.262	7.092
SHAH	3	1.0	0.283	16.813
HHAH	4	1.0	0.387	3.190
OHAH	4	1.0	0.299	3.685
IHAH	4	1.0	0.314	3.682
SHAH	4	1.0	0.339	8.629
HHAH	5	1.0	0.310	4.381
OHAH	5	1.0	0.374	5.142
IHAH	5	1.0	0.393	3.854
SHAH	5	1.0	0.424	8.498
HHAH	6	1.0	0.258	3.906
OHAH	6	1.0	0.499	3.812
IHAH	6	1.0	0.524	3.307
SHAH	6	1.0	0.565	8.056

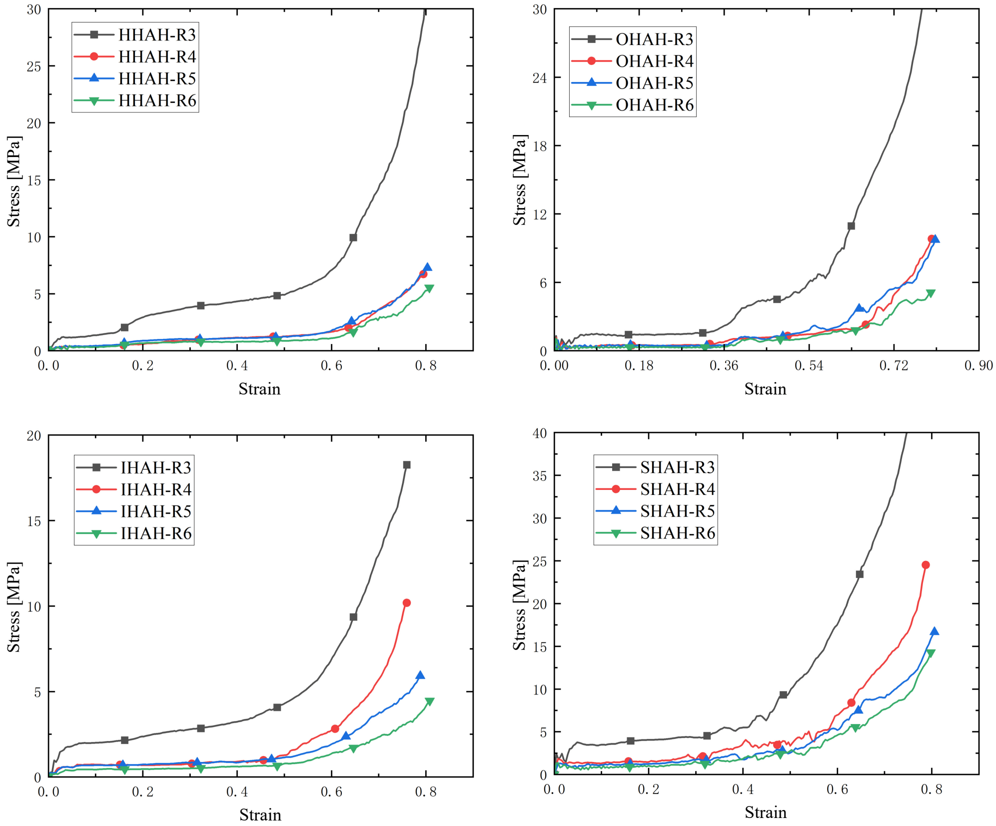

Fig. 22. Stress-strain curves with different cylindrical radii: (a) HHAH, (b) OHAH, (c) IHAH, (d) SHAH.

which led to premature compression and mutual collisions between different parts during loading.

For the other radius values, prior to entering the densification stage, the strain differences between the structures were negligible. After reaching the densification stage (approximately $\varepsilon = 0.65$), notable changes in stress occurred in the IHAH and SHAH structures. Specifically, as the radius increased, the force required for structural collapse decreased.

Figure 23 and Table 3 present the SEA of honeycomb structures with different inscribed circle radii. As illustrated in Fig. 23, the SEA of the HHAH and OHAH structures exhibited an initial decrease, followed by an increase, and a subsequent decrease. In contrast, the SEA values of IHAH and SHAH (except for $R = 3$ mm) remained relatively similar across the different radii. This indicates that the effect of the radius variation differs according to the specific structural configuration.

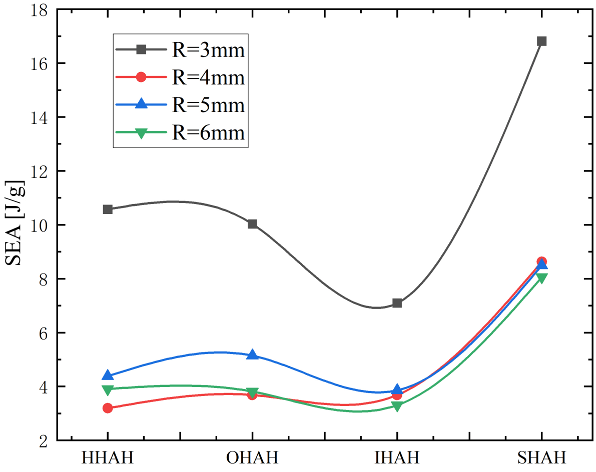

FIG. 23. SEA with different cylindrical radii.

Notably, the SEA of the SHAH consistently surpassed that of the other honeycomb types, demonstrating the most effective energy absorption performance among them.

The data in Table 3 clearly demonstrate that topology dominates the relative density in determining the SEA. For example, at $R = 3$ mm, the SHAH structure has a relatively low relative density ($\bar{\rho} = 0.283$) but achieved the highest SEA (16.81 J/g) of all configurations. In contrast, the HHAH structure at the same R has a much higher relative density ($\bar{\rho} = 0.516$) but a significantly lower SEA (10.57 J/g). This indicates that the staggered arrangement pattern (SHAH) provides an intrinsic topological advantage that outweighs the effects of a higher density. A similar trend is observed at other radii, e.g., at $R = 5$ mm, SHAH ($\bar{\rho} = 0.424$, SEA = 8.50 J/g) outperforms OHAH ($\bar{\rho} = 0.374$, SEA = 5.14 J/g) and IHAH ($\bar{\rho} = 0.393$, SEA = 3.85 J/g), despite having a comparable or even lower relative density in some cases.

5.3. Effect of the cell numbers

The number of honeycomb cells is a key factor influencing the mechanical properties and deformation behavior of honeycomb materials. This section systematically analyzes the mechanical performance of honeycomb specimens with different cell numbers. Four different numbers of unit cells were set for each configuration to investigate the effect of cell size on the mechanical properties. Based on the distribution of cell counts, the specimens were divided into four groups (Table 4): small-cell group (Group S), medium-cell group (Group M), large-cell group (Group L), and transitional-cell group (Group T).

Figure 24 shows the stress-strain curves of the different honeycomb specimens with varying unit cell counts during deformation. As shown in Fig. 24, the stress values differed slightly across different cell counts, indicating that the design of the cell number had a limited impact on the overall mechanical performance of the structure.

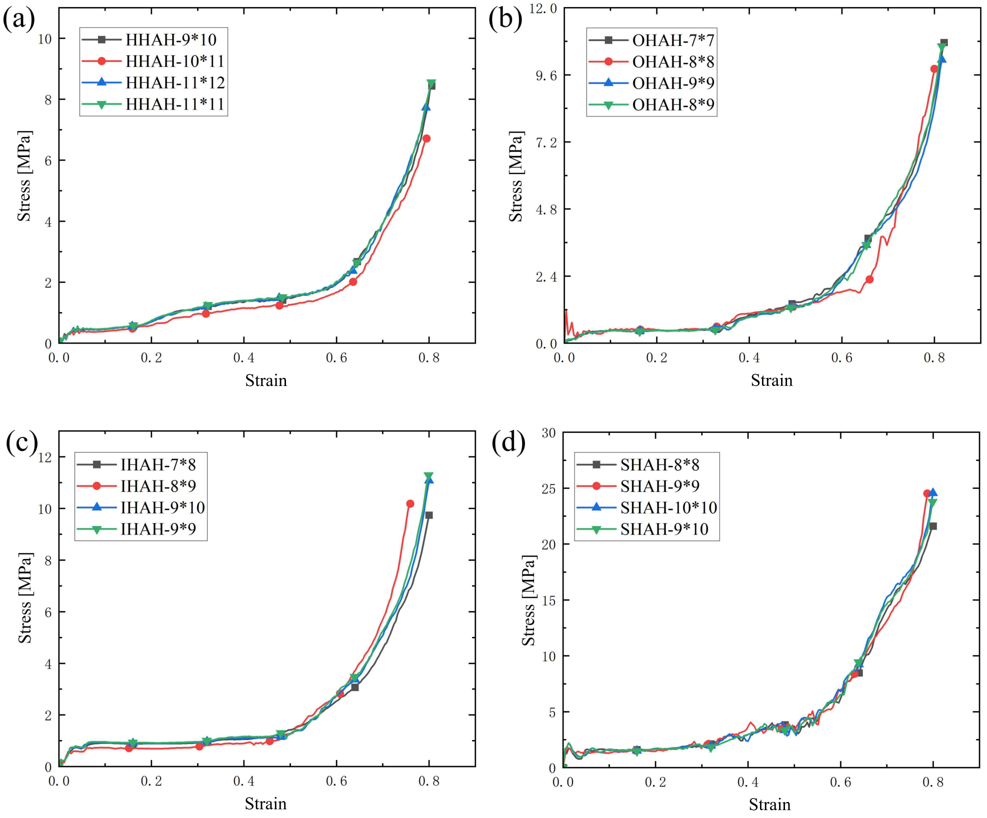

FIG. 24. Stress-strain curves with different cell numbers:
(a) HHAH, (b) OHAH, (c) IHAH, (d) SHAH.

Figure 25 shows the SEA of the different honeycomb types, which are detailed in Table 4. Observations from Fig. 25 reveal that the SEA of all honeycomb structures initially decreased and then increased with the number of cells. A further comparison between Groups L and T (i.e., reducing one set of cells in the horizontal direction) showed a slight increase in SEA for all honeycomb structures. When the cell count corresponded to that of Group T, the SEA of the other three honeycomb types reached a maximum, except for that of SHAH. Under identical conditions, SHAH consistently exhibits the highest SEA value. Overall, appropriately reducing the number of cells in the horizontal

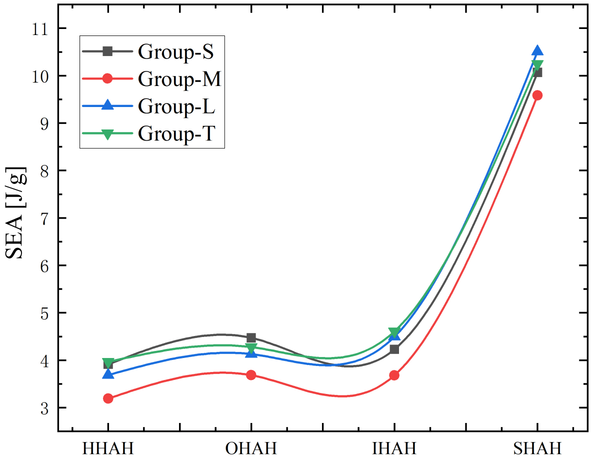

Fig. 25. SEA with different cell numbers.

direction enhanced the specific energy absorption performance of the honeycomb structure.

As shown in Table 4, the relative density of each topology is nearly constant across different cell-number groups (e.g., SHAH $\bar{\rho} \approx 0.424$, HHAH $\bar{\rho} \approx 0.387$, etc.), the observed differences in SEA can be attributed primarily to the topo-

Table 4. Parameters and SEA values of the five types of honeycombs with different cell numbers.

Honeycombs	R [mm]	N [mm]	t [mm]	$\bar{\rho}$	SEA [J/g]
HHAH	4	9*10(S)	1.0	0.387	3.913
OHAH	4	7*7(S)	1.0	0.374	4.472
IHAH	4	7*8(S)	1.0	0.393	4.230
SHAH	4	8*8(S)	1.0	0.424	10.070
HHAH	4	10*11(M)	1.0	0.387	3.190
OHAH	4	8*8(M)	1.0	0.374	3.685
IHAH	4	8*9(M)	1.0	0.393	3.682
SHAH	4	9*9(M)	1.0	0.424	9.582
HHAH	4	11*12(L)	1.0	0.387	3.686
OHAH	4	9*9(L)	1.0	0.374	4.129
IHAH	4	9*10(L)	1.0	0.393	4.500
SHAH	4	10*10(L)	1.0	0.424	10.509
HHAH	4	11*11(T)	1.0	0.387	3.966
OHAH	4	8*9(T)	1.0	0.374	4.277
IHAH	4	9*9(T)	1.0	0.393	4.608
SHAH	4	9*10(T)	1.0	0.424	10.248

logical arrangement pattern rather than relative density. For example, in the S group (small cell count), SHAH achieved an SEA of 10.07 J/g, which is approximately 2.3–2.7 times higher than those of HAH (3.91 J/g), OHAH (4.47 J/g), and IHAH (4.23 J/g), despite having only a slightly higher relative density. In the L group (large cell count), SHAH (10.51 J/g) again far exceeds the other three topologies (3.69–4.50 J/g). These results confirm that the staggered arrangement pattern (SHAH) provides a substantial topology-dependent advantage for energy absorption, independent of the relative density. The minor variations in the SEA for each topology across different cell numbers indicate that the cell number has a secondary effect compared to the topology.

5.4. Effect of the rib plate ratio

This section investigates the influence of the outer-to-inner arm length ratio (H_1/H_2) on the mechanical performance of the SHAH. In previous studies, the H_1/H_2 ratio was fixed at 1. To further analyze the strengthening mechanism of the local hexa-arm honeycombs, the mechanical responses of the SHAH structures with different H_1/H_2 ratios were analyzed.

The stress-strain curves shown in Fig. 26 indicate that the mechanical performance of the hexa-arm honeycomb is influenced by the unit cell arrangement and strongly depends on the arm length ratio. When the outer arm length is excessively large (e.g., $H_1/H_2 = 3$), the supporting effect of the arms weakens, leading to a reduced load-bearing capacity. For $H_1/H_2 = 0.6$ and 1, the performances in the initial compression stage were similar. After entering the second plateau

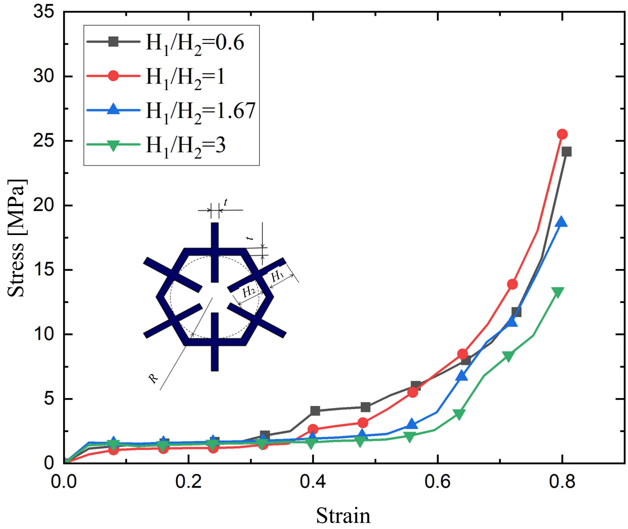

Fig. 26. Stress-strain curves for SHAH structures with different arm length ratios.

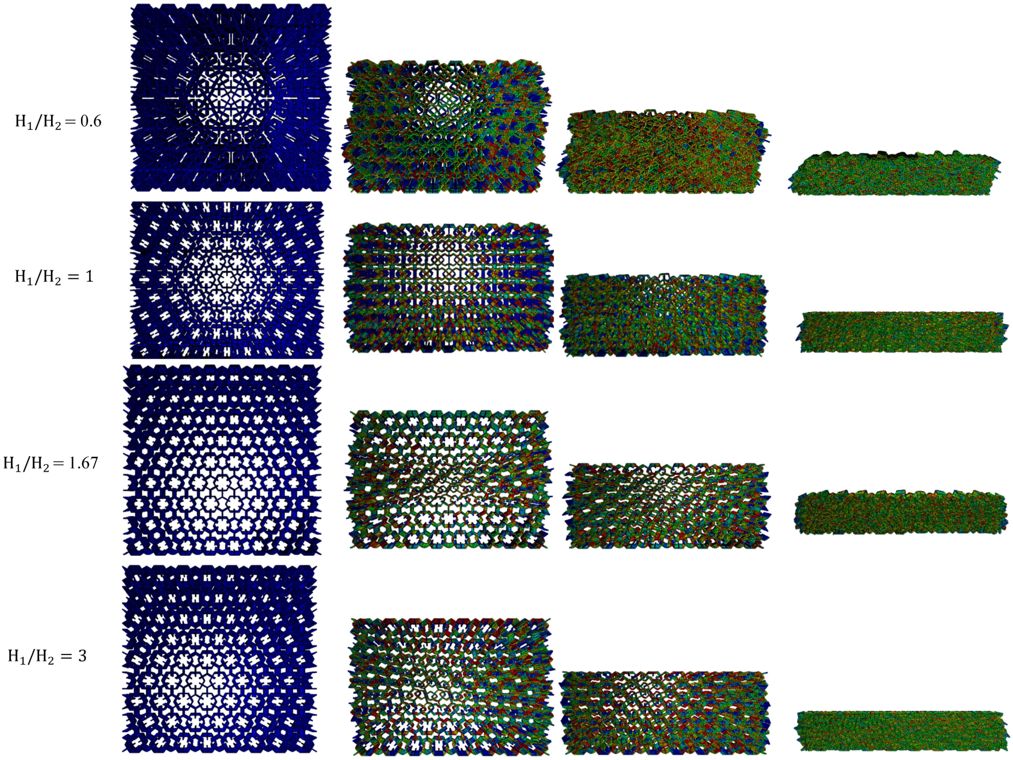

FIG. 27. Deformation processes for SHAH structures with different arm length ratios.

stage, a ratio of 0.6 performed slightly better than 1. However, upon entering the densification stage, the load-bearing capacity was the highest at a ratio of 1. The deformation processes shown in Fig. 27 indicate that the compression deformation processes differ for different arm ratios. When H_1/H_2 was 0.6, the compression deformation exhibited a lateral offset, and the deformation was global. When $H_1/H_2 = 1$, the compression deformation was uniformly horizontal and relatively stable. The deformation processes for H_1/H_2 ratios of 1.67 and 3 were quite similar, both showing initial significant deformation in the central part, which then propagated towards the upper and lower sections, indicating a characteristic transition from local buckling.

6. Conclusion

To design honeycomb metamaterial structures with excellent energy absorption characteristics and high load-bearing capacity, this study proposes and investigates four novel hexa-arm honeycomb configurations. Their mechanical behavior under quasi-static compression was systematically studied using the combined experimental and numerical simulation approach. Through a comparative analysis of the in-plane compressive performance and deformation processes of the four honeycomb structures, the following conclusions were drawn.

(1) The hexa-arm honeycombs exhibited two elastic stages, which allowed them to possess higher plateau stresses, resulting in better load-bearing capacity and energy absorption capability.

(2) All the hexa-arm honeycombs exhibited superior mechanical performance, which was dependent on the arrangement pattern. In the compression direction, the deformation modes of the hexa-arm honeycomb varied according to the arrangement pattern. A common feature of all hexa-arm honeycombs is that they do not exhibit shear band collapse, and the entire structure deforms collectively, with the hexagonal honeycomb cells undergoing elastic shape changes. During compression, each cell resists changes in its shape and maintains its shape. In contrast, the collapse of the HHAH and IHAH was initiated from the shear band direction, with slight bending observed in the final stage. In contrast, OHAH and SHAH underwent a progressive layer-by-layer collapse during the compression deformation, which occurred later.

(3)Among the arrangement patterns of the hexa-arm honeycombs, the SHAH structure exhibited the best mechanical performance, followed by the IHAH structure. The OHAH and HHAH structures were similar to one another. The applied pressure can be transmitted through these arms to every cell, enabling all units to collectively resist changes in shape. This allows the hexa-arm honeycombs to absorb more energy and degrade stably.

(4) Owing to the increase in the material, the enhancement in wall thickness significantly improved the energy absorption performance of different honeycomb structures. When the wall thickness increased from 0.6 to 1.2 mm, the SEA of HHAH, OHAH, IHAH, and SHAH increased by 179.6%, 190.5%, 171.9%, and 162.1%, respectively.

For honeycombs with different structural configurations, as the inscribed circle radius R increased, the SEA of HHAH and OHAH exhibited a trend of initially decreasing, then increasing, and subsequently decreasing. In contrast, the SEA values of IHAH and SHAH remained relatively similar under the other radius conditions, except for $R = 3$ mm.

Under quasi-static compression conditions, when the number of cells in both the horizontal and vertical directions of the honeycomb structure simultaneously increased, the SEA of all honeycomb structures initially decreased and then increased with the total number of cells. However, when only one set of cells in the horizontal direction was reduced, the SEA of all honeycomb structures improved.

(5) The influence of the outer-to-inner arm length ratio on the in-plane compressive performance of the SHAH structure was investigated. The results indi-

cated that the mechanical performance of the hexa-arm honeycomb was influenced by the unit cell arrangement and strongly depended on the arm length ratio. When the outer arm length is excessively large (e.g., $H_1/H_2 = 3$), the supporting effect of the arms weakens, leading to a reduced load-bearing capacity. For $H_1/H_2 = 0.6$ and 1, the performance in the initial compression stage was similar. After entering the second plateau stage, a ratio of 0.6 performed slightly better than 1. However, upon entering the densification stage, the load-bearing capacity was the highest at a ratio of 1.

(6) Quantitative validation confirms good agreement between experiments and simulations: relative errors for peak stress, plateau stress, SEA, and densification strain are all below 10%, and the experimental repeatability is high (coefficient of variation <5%). Compared with a conventional hexagonal honeycomb of the same relative density, SHAH shows a 660% higher plateau stress and up to 155% higher SEA, confirming the mechanical advantage of the hexa-arm topology. All four hexa-arm honeycombs exhibit positive Poisson's ratios, with SHAH having the highest value, indicating a distinctive lateral deformation behavior.

This study revealed the relationship between the geometric configuration and arrangement of honeycomb structures and their in-plane compression performance. Future research could incorporate multi-condition loading scenarios to further expand the application potential of such structures in terms of their impact resistance and energy absorption. The findings not only provide a new direction for developing honeycomb metamaterials with a high energy absorption capacity but also offer a novel design approach for enhancing the performance of porous materials.

CRediT authorship contribution statement

Wensheng Wang: Funding acquisition, Methodology, Supervision, Resources, Writing – original draft. Yichen Zhang: Data curation, Formal analysis, Visualization. Xinyu Song: Software, Project administration, Writing – review & editing.

Declaration of competing interest

The authors declare that they have no competing financial interests or personal relationships that could influence the work reported in this study.

Data availability

The datasets generated and/or analyzed during the current study are available from the corresponding author upon reasonable request.

Acknowledgments

This research was supported by the National Natural Science Foundation of China (Grant No. 51975187), State Key Laboratory of Structural Analysis, Optimization and CAE Software for Industrial Equipment (GZ25108).

References

1. Z.G. Wang, *Recent advances in novel metallic honeycomb structure*, Composites Part B: Engineering, **166**, 731–741, 2019, https://doi.org/10.1016/j.compositesb.2019.02.011.
2. S. Li, R. Yang, S. Sun, B. Niu, *Advances in the analysis of honeycomb structures: A comprehensive review*, Composites Part B: Engineering, **296**, 112208, 2025, https://doi.org/10.1016/j.compositesb.2025.112208.
3. E.T. Zhang, H. Liu, B.F. Ng, *Novel arc-shaped ligaments to enhance energy absorption capabilities of re-entrant anti-trichiral structures*, Composites Part B: Engineering, **227**, 109366, 2021, https://doi.org/10.1016/j.compositesb.2021.109366.
4. S. Chen, X. Tan, J. Hu, S. Zhu, B. Wang, L. Wang, Y. Jin, L. Wu, *A novel gradient negative stiffness honeycomb for recoverable energy absorption*, Composites Part B: Engineering, **215**, 108745, 2021, https://doi.org/10.1016/j.compositesb.2021.108745.
5. M. Kucewicz, P. Baranowski, J. Małachowski, A. Popławski, P. Płatek, *Modeling and characterization of 3D printed cellular structures*, Materials & Design, **142**, 177–189, 2018, https://doi.org/10.1016/j.matdes.2018.01.028.
6. T. Akash, K. Raman, J.C. Singh, *A review on characteristics of composite and advanced materials used for aerospace applications*, Materials Today: Proceedings, **51**, Part 1, 865–870, 2022, https://doi.org/10.1016/j.matpr.2021.06.276.
7. G. Sun, X. Huo, H. Wang, P.J. Hazell, Q. Li, *On the structural parameters of honeycomb-core sandwich panels against low-velocity impact*, Composites Part B: Engineering, **216**, 108881, 2021, https://doi.org/10.1016/j.compositesb.2021.108881.
8. Y. Garbatov, S.S. Marchese, G. Epasto, V. Crupi, *Flexural response of additive-manufactured honeycomb sandwiches for marine structural applications*, Ocean Engineering, **302**, 117732, 2024, https://doi.org/10.1016/j.oceaneng.2024.117732.
9. G. Palomba, G. Epasto, L. Sutherland, V. Crupi, *Aluminium honeycomb sandwich as a design alternative for lightweight marine structures*, Ships and Offshore Structures, **17**, 10, 2355–2366, 2022, https://doi.org/10.1080/17445302.2021.1996109.
10. K.B. Shin, J.Y. Lee, S.H. Cho, *An experimental study of low-velocity impact responses of sandwich panels for Korean low floor bus*, Composite Structures, **84**, 3, 228–240, 2008, https://doi.org/10.1016/j.compstruct.2007.08.002.
11. H. Mozafari, S. Khatami, H. Molatefi, *Out of plane crushing and local stiffness determination of proposed foam filled sandwich panel for Korean Tilting Train eXpress-Numerical study*, Materials & Design, **66**, Part B, 400–411, 2015, https://doi.org/10.1016/j.matdes.2014.07.037.
12. C. Qi, F. Jiang, S. Yang, *Advanced honeycomb designs for improving mechanical properties: A review*, Composites Part B: Engineering, **227**, 109393, 2021, https://doi.org/10.1016/j.compositesb.2021.109393.

13. S.R. Dhari, *Influence of material plasticity and bimodularity on the compressive response of fused-filament fabricated re-entrant honeycombs*, Modelling and Simulation in Materials Science and Engineering, **34**, 015019, 2026, https://doi.org/10.1088/1361-651X/ae33d6.

14. Q. Zhang, X. Yang, P. Li, G. Huang, S. Feng, C. Shen, B. Han, X. Zhang, F. Jin, F. Xu, T.J. Lu, *Bioinspired engineering of honeycomb structure – Using nature to inspire human innovation*, Progress in Materials Science, **74**, 332–400, 2015, https://doi.org/10.1016/j.pmatsci.2015.05.001.

15. W. Wu, W. Hu, G. Qian, H. Liao, X. Xu, F. Berto, *Mechanical design and multifunctional applications of chiral mechanical metamaterials: A review*, Materials & Design, **180**, 107950, 2019, https://doi.org/10.1016/j.matdes.2019.107950.

16. A. Schiavone, G. McShane, *Compressive collapse modes of hyperelastic origami honeycombs*, Mechanics of Materials, **215**, 105600, 2026, https://doi.org/10.1016/j.mechmat.2026.105600.

17. Z. Wang, C. Luan, G. Liao, J. Liu, X. Yao, J. Fu, *Progress in auxetic mechanical metamaterials: Structures, characteristics, manufacturing methods, and applications*, Advanced Engineering Materials, **22**, 10, 2000312, 2020, https://doi.org/10.1002/adem.202000312.

18. A. Ingrole, A. Hao, R. Liang, *Design and modeling of auxetic and hybrid honeycomb structures for in-plane property enhancement*, Materials & Design, **117**, 72–83, 2017, https://doi.org/10.1016/j.matdes.2016.12.067.

19. D.Q. Wu, Z.Y. Xu, D.Z. Guo, Z. Yuan, E. Wu, L. Lu, W. Wu, Z. Zhang, *Research on the design and mechanical performance of additively manufactured diamond plate lattice metamaterials*, Polymer Composites, **46**, S1, S836–S855, 2025, https://doi.org/10.1002/pc.29819.

20. T. Wang, Z. Li, L. Wang, G.M. Hulbert, *Crashworthiness analysis and collaborative optimization design for a novel crash-box with re-entrant auxetic core*, Structural and Multidisciplinary Optimization, **62**, 2167–2179, 2020, https://doi.org/10.1007/s00158-020-02568-6.

21. D.A. Debeau, C.C. Seepersad, M.R. Haberman, *Impact behavior of negative stiffness honeycomb materials*, Journal of Materials Research, **33**, 3, 290–299, 2018, https://doi.org/10.1557/jmr.2018.7.

22. S.N. Ha, G. Lu, *A review of recent research on bio-inspired structures and materials for energy absorption applications*, Composites Part B: Engineering, **181**, 107496, 2020, https://doi.org/10.1016/j.compositesb.2019.107496.

23. N.K. Choudhry, B. Panda, S. Kumar, *In-plane energy absorption characteristics of a modified re-entrant auxetic structure fabricated via 3D printing*, Composites Part B: Engineering, **228**, 109437, 2022, https://doi.org/10.1016/j.compositesb.2021.109437.

24. C.O. Ufodike, M.F. Ahmed, G. Dolzyk, *Additively manufactured biomorphic cellular structures inspired by wood microstructure*, Journal of the Mechanical Behavior of Biomedical Materials, **123**, 104729, 2021, https://doi.org/10.1016/j.jmbbm.2021.104729.

25. D. Köllner, B. Tolve-Granier, S. Simon, K.I. Kakimoto, T. Fey, *Advanced estimation of compressive strength and fracture behavior in ceramic honeycombs by polarimetry measurements of similar epoxy resin honeycombs*, Materials, **15**, 7, 2361, 2022, https://doi.org/10.3390/ma15072361.

26. T. Chatterjee, S. Chakraborty, S. Goswami, S. Adhikari, M.I. Friswell, *Robust topological designs for extreme metamaterial micro-structures*, Scientific Reports, **11**, 1, 15221, 2021, https://doi.org/10.1038/s41598-021-94520-x.

27. S. Saurabh, A. Gupta, R. Chowdhury, *Impact of parametric variation to achieve extreme mechanical metamaterials through topology optimization*, Composite Structures, **326**, 117611, 2023, https://doi.org/10.1016/j.compstruct.2023.117611.

28. A. Gupta, A. Gupta, R. Chowdhury, *Computational design of auxetic microstructures via stress-based topology optimization*, Engineering Structures, **319**, 118807, 2024, https://doi.org/10.1016/j.engstruct.2024.118807.

29. G. Agrawal, A. Gupta, R. Chowdhury, A. Chakrabarti, *Robust topology optimization of negative Poisson's ratio metamaterials under material uncertainty*, Finite Elements in Analysis and Design, **198**, 103649, 2022, https://doi.org/10.1016/j.finel.2021.103649.

30. R.S.G. Bates, I.R. Farrow, R.S. Trask, *Compressive behaviour of 3D printed thermoplastic polyurethane honeycombs with graded densities*, Materials & Design, **162**, 130–142, 2019, https://doi.org/10.1016/j.matdes.2018.11.019.

31. N. Novak, L. Starčevič, M. Vesenjak, Z. Ren, *Blast response study of the sandwich composite panels with 3D chiral auxetic core*, Composite Structures, **210**, 167–178, 2019, https://doi.org/10.1016/j.compstruct.2018.11.043.

32. Y.Y. Chen, T.T. Li, Z. Jia, F. Scarpa, C.W. Yao, L.F. Wang, *3D printed hierarchical honeycombs with shape integrity under large compressive deformations*, Materials & Design, **137**, 226–234, 2018, https://doi.org/10.1016/j.matdes.2017.10.028.

33. C. Qi, A. Remennikov, L. Pei, S. Yang, Z.H. Yu, T.D. Ngo, *Impact and close-in blast response of auxetic honeycomb-cored sandwich panels: Experimental tests and numerical simulations*, Composite Structures, **180**, 161–178, 2017, https://doi.org/10.1016/j.compstruct.2017.08.020.

34. Z. Dong, Y. Li, T. Zhao, W. Wu, D. Xiao, J. Liang, *Experimental and numerical studies on the compressive mechanical properties of the metallic auxetic re-entrant honeycomb*, Materials & Design, **182**, 108036, 2019, https://doi.org/10.1016/j.matdes.2019.108036.

35. T. Simsek, Z. Evis, *Additive manufacturing of overexpanded honeycomb core lattice structures and their characterization*, Materials Testing, **67**, 9, 1545–1556, 2025, https://doi.org/10.1515/mt-2025-0058.

36. G. Arquilla, A. Ceci, G. Costanza, M.E. Tata, *Effect of the load application angle on the compressive behavior of AI honeycomb under combined normal-shear stress*, Materials, **16**, 15, 5462, 2023, https://doi.org/10.3390/ma16155462.

37. M. Yu, Z. Wang, L. Song, X. Jiang, S. Zhao, L. Geong, D. Sun, *Out-of-plane compression properties of a lightweight, high-strength and sustainable bamboo honeycomb sandwich structural material*, Journal of Cleaner Production, **498**, 145217, 2025, https://doi.org/10.1016/j.jclepro.2025.145217.

38. R.J. Moat, E. Muyupa, C. Imediegwu, D.J. Clarke, I. Jowers, U.G. Grimm, *Compressive behaviour of cellular structures with aperiodic order*, Results in Materials, **15**, 100293, 2022, https://doi.org/10.1016/j.rinma.2022.100293.

39. T. Shen, B. Li, *Design of non-homogeneous three-dimensional ceramic lattice structures with interpenetrating epoxy resin for enhanced energy absorption and load-bearing*

performance, Mechanics of Advanced Materials and Structures, **33**, 1, 2448298, 2026, https://doi.org/10.1080/15376494.2024.2448298.

40. C. Gao, J. Shi, H. Tang, H. Tang, Z. Xiao, Y. Bi, Z. Liu, J.H. Rao, *Mechanical properties and energy absorption capabilities of plate-based AlSi10Mg metamaterials produced by laser powder bed fusion*, Journal of Materials Research and Technology, **30**, 3851–3862, 2024, https://doi.org/10.1016/j.jmrt.2024.04.114.

41. X. Wang, Z. Yan, S. Guo, Y. Zhang, C. Liu, Z. Liu, *Enhancing compressive mechanical properties of anisotropic shell-based architected materials*, Composite Structures, **367**, 119240, 2025, https://doi.org/10.1016/j.compstruct.2025.119240.

42. L.J. Gibson, M.F. Ashby, *Cellular Solids: Structure and Properties*, Cambridge University Press, 1997, https://doi.org/10.1017/cbo9781139878326.

43. K.M. Yadav, K. Praveenkumar, R.H. Shukla, S. Nilawar, C.S. Perugu, K. Chatterjee, S. Suwas, J. Jayaraj, K.G. Prashanth, *Novel partially biodegradable Ti-6Al-4V/Zn composites fabricated through hybrid additive manufacturing and powder metallurgy*, Advanced Light Materials, **1**, 1, 1–18, 2026, https://doi.org/10.1016/j.almate.2026.03.001.

44. Y. Sun, Q. Chen, N. Pugno, *Elastic and transport properties of the tailorable multifunctional hierarchical honeycombs*, Composite Structures, **107**, 698–710, 2014, https://doi.org/10.1016/j.compstruct.2013.07.012.

45. A. Álvarez-Trejo, E. Cuan-Urquizo, D. Bhate, A. Roman-Flores, *Mechanical metamaterials with topologies based on curved elements: An overview of design, additive manufacturing and mechanical properties*, Materials & Design, **233**, 112190, 2023, https://doi.org/10.1016/j.matdes.2023.112190.

46. S. Yin, H. Chen, J. Li, T.X. Yu, J. Xu, *Effects of architecture level on mechanical properties of hierarchical lattice materials*, International Journal of Mechanical Sciences, **157–158**, 282–292, 2019, https://doi.org/10.1016/j.ijmecsci.2019.04.051.

47. X. Wang, P. Zhang, S. Ludwick, E. Belski, A.C. To, *Natural frequency optimization of 3D printed variable-density honeycomb structure via a homogenization-based approach*, Additive Manufacturing, **20**, 189–198, 2018, https://doi.org/10.1016/j.addma.2017.10.001.

48. Y. Qiu, J.S. Wang, *Research progress on phase-field simulation of rapid solidification in additive manufacturing* [in Chinese], Aeronautical Manufacturing Technology, **16**, 50–58, 2020, https://doi.org/10.16080/j.issn1671-833x.2020.16.050.

49. H.N.G. Wadley, N.A. Fleck, A.G. Evans, *Fabrication and structural performance of periodic cellular metal sandwich structures*, Composites Science and Technology, **63**, 16, 2331–2343, 2003, https://doi.org/10.1016/S0266-3538(03)00266-5.

50. D. Mondal, T. Garai, G.C. Roy, S. Alam, *Describing a logistic model for the generation of methane from coal through the interval fuzzy numbers*, Springer Nature Operations Research Forum, **6**, 3, 114, 2025, https://doi.org/10.1007/s43069-025-00518-w.

51. X.L. Guo, B.H. Sun, Reinforced design and temperature-varying compressive performance investigation of aperiodic honeycomb metamaterials, Composite Structures, **372**, 119541, 2025, https://doi.org/10.1016/j.compstruct.2025.119541.

52. P. Xia, Q. Liu, H. Fu, Y. Yu, L. Wang, Q. Wang, X. Yu, F. Zhao, *Mechanical properties and energy absorption of 3D printed double-layered helix honeycomb under in-plane compression*, Composite Structures, **315**, 116982, 2023, https://doi.org/10.1016/j.compstruct.2023.116982.

53. J. Khaghanifard, R. Ansarian, R. Talebitooti, *Enhancing output performance of a functionally graded magneto-electro-elastic energy harvester using a re-entrant honeycomb auxetic core and variable cross-section*, Archive of Applied Mechanics, **96**, 69, 2026, https://doi.org/10.1016/j.compstruct.2023.116982.

54. Q. Lu, X. Deng, *Energy absorption and in-plane mechanical behavior of honeycomb structures with reinforced strut*, Composite Structures, **322**, 117399, 2023, https://doi.org/10.1016/j.compstruct.2023.117399.

55. X. Deng, S. Qin, J. Huang, *Out-of-plane impact analysis for a bioinspired sinusoidal honeycomb*, Mechanics of Advanced Materials and Structures, **29**, 28, 7259–7276, 2021, https://doi.org/10.1080/15376494.2021.1995547.

56. R. Zhong, X. Ren, X. Yu Zhang, C. Luo, Y. Zhang, Y.M. Xie, *Mechanical properties of concrete composites with auxetic single and layered honeycomb structures*, Construction and Building Materials, **322**, 126453, 2022, https://doi.org/10.1016/j.conbuildmat.2022.126453.

57. S. Tabacu, N.D. Stanescu, *A theoretical model for the estimate of the reaction force for 3D auxetic anti-tetra chiral tubular structures under tensile loads*, Thin-Walled Structures, **168**, 108304, 2021, https://doi.org/10.1016/j.tws.2021.108304.

58. R.Z. Lu, J.C. Zeng, C.B. Cui, Q. Zhang, Y. Li, J. Feng, M. Li, J. Cai, *Fracture behavior and enhancement of crash cushion with bolted reinforced honeycomb under large deformation*, Engineering Structures, **341**, 120832, 2025, https://doi.org/10.1016/j.engstruct.2025.120832.

59. N. Pagliocca, G. Youssef, B. Koohbor, *In-plane mechanical and failure responses of honeycombs with syntactic foam cell walls*, Composite Structures, **295**, 115866, 2022, https://doi.org/10.1016/j.compstruct.2022.115866.

60. J. Wang, H. Yang, Z. Li, Y. Xie, J. Gao, F. Chen, H. Lan, *Development and validation of an equivalent honeycomb model*, Thin-Walled Structures, **210**, 113058, 2025, https://doi.org/10.1016/j.tws.2026.114632.

61. K. Siwek, K. Spychel, M. Kucewicz, P. Baranowski, *Efficient numerical simulation of compression behaviour of SLA 3D printed cellular structures*, Thin-Walled Structures, **223**, 114632, 2026, https://doi.org/10.1016/j.tws.2026.114632.

Received February 8, 2026; revised version April 26, 2026.